Characterizing Equatorial waves in the Atmosphere under different mean states

A Thesis

submitted to
Indian Institute of Science Education and Research Pune
in partial fulfillment of the requirements for the
BS-MS Dual Degree Programme

by

Athul R S
20131031

IISER PUNE

Indian Institute of Science Education and Research Pune
Dr. Homi Bhabha Road,
Pashan, Pune 411008, INDIA.

May, 2018

Supervisor: Dr. Neena Joseph Mani
ECS Department

Certificate

This is to certify that this dissertation entitled “Characterizing Equatorial waves in the Atmosphere under different mean states” towards the partial fulfillment of the BS-MS dual degree programme at the Indian Institute of Science Education and Research, Pune represents study/work carried out by Athul R S at Indian Institute of Science Education and Research, Pune under the supervision of Dr. Neena Joseph Mani, Assistant Professor, ECS Department, during the academic year 2017-2018.

Student

Athul R S

Supervisor

Dr Neena Joseph Mani

Committee:

Name of your Guide: Dr. Neena Joseph Mani

Name of your TAC : Dr. Suhas Ettammal

Declaration

I hereby declare that the matter embodied in the report entitled "Characterizing Equatorial waves in the Atmosphere under different mean states" are the results of the work carried out by me at the ECS Department, Indian Institute of Science Education and Research, Pune, under the supervision of Dr. Neena Joseph Mani and the same has not been submitted elsewhere for any other degree.

Student

Athul R S

Supervisor

Dr Neena Joseph Mani

Acknowledgments

I would like to express my gratitude to everyone who has helped me perform the works necessary for this thesis in the past year.

First of all, I would like thank Dr. Neena Joseph Mani with whom I have been working for the past two years, for her priceless guidance and timely advises that directed me towards my goals. She was always approachable and has been very patient in helping me clear my doubts. I have been nothing less that blessed to have got an opportunity to work with an advisor like Dr. Neena who let me work at my own pace but always made sure that I stay focused and achieve the goals.

I would like to thank my TAC Dr. Suhas Ettammal for his valuable remarks during the mid-year evaluation that have helped me improve the results.

I would like thank our lab members who have always been very friendly and discussions with them have always been fun and informative.

Finally, I would like to express my deep gratitude to my family members and friends, for their support and for believing in me during tough times.

Sincerely,
Athul R S

Abstract

Convectively coupled equatorial waves serves as the primary source of information for understanding the highly coupled ocean-atmosphere system. Since the spatio-temporal scales of equatorial waves fall conveniently between those of weather and climate, they can influence both the scales. In this study we plan to focus on the effect of mean states on equatorial waves to better understand the interaction of equatorial waves with weather and climate scales under different background conditions. They study may provide important insight on equatorial wave dynamics in a warming environment.

Chapter 1: Space time spectral analysis was performed on daily OLR and U850 data to identify the spectral signatures of equatorial waves. Coherence-squared spectra was also performed on OLR with U850 to study the correlation between the equatorial wave signals in OLR and U850. Further wave-filtered OLR was used to locate the active regions of equatorial wave activity. Preferential peaking of equatorial wave activities during different phases of ENSO was identified.

Chapter 2: Vertical propagation of equatorial waves under different background states was studied. Linear regression technique and Empirical Orthogonal Function analysis were used to identify the convective patterns of equatorial waves. Preferential vertical propagation of equatorial waves during different phases of QBO was identified.

Chapter 3: OLR, U850 and U200 data from five global climate models that efficiently simulate MJO are compared with observation results to observe how well these models simulate convectively coupled equatorial waves in the troposphere, using the same analysis performed in Chapter 1.

Contents

List of Figures

List of Tables

Chapter 1

Influence of Mean State on Atmospheric Equatorial Waves

1.1 Background: Theory of Convectively Coupled Equatorial Waves

1.1.1 Shallow Water Theory

Matsuno[1966] was the first to develop a comprehensive theoretical background explaining the dynamics of Equatorial Waves. He assumed a layer of incompressible fluid with a free surface which is under hydrostatic balance.

The equatorial atmosphere was assumed to be barotropic in nature with constant pressure surfaces parallel to constant density surfaces. Momentum and mass conservation can be written as:

$$\frac{\partial u}{\partial t} - fv + \frac{\partial \phi}{\partial x} = 0, \tag{1.1}$$

$$\frac{\partial v}{\partial t} + fu + \frac{\partial \phi}{\partial y} = 0, \tag{1.2}$$

$$\frac{\partial \phi}{\partial t} + gh_e(\frac{\partial u}{\partial x} + \frac{\partial v}{\partial y}) = 0, \tag{1.3}$$

where, *u* and *v* are velocities in the eastward and northward directions respectively, ϕ is geopotential, *t* is time, *g* is the acceleration due to gravity, *f* is the *Coriolis parameter*, and h_e is the depth of the undisturbed layer. Under *Beta-plane* approximation, *f* varies proportional to the distance from the equator as:

$$f = \beta y, \tag{1.4}$$

where, β(called the *Rossby* parameter) is defined as the latitudinal gradient of *f*.

We are interested in the zonally propagating wave solutions of the form:

$$\begin{bmatrix} u \\ v \\ \phi \end{bmatrix} = \begin{bmatrix} \hat{u}(y) \\ \hat{v}(y) \\ \hat{\phi}(y) \end{bmatrix} \times exp[i(kx - \omega t)], \tag{1.5}$$

where, *k* is the zonal wave number, ω is the frequency and $\hat{u}$, $\hat{v}$ and $\hat{\phi}$ define the meridional structure of *u*,*v* and ϕ respectively. Solving for $\hat{v}$, we get:

$$\frac{\partial^2 \hat{v}}{\partial y^2} + (\frac{\omega^2}{gh_e} - k^2 - \frac{k}{\omega}\beta - \frac{\beta^2 y^2}{gh_e})\hat{v} = 0. \tag{1.6}$$

It follows that the part inside the parentheses must satisfy the following condition:

$$\frac{\sqrt{gh_e}}{\beta}(\frac{\omega^2}{gh_e} - k^2 - \frac{k}{w}\beta) = 2n + 1 \qquad ; n = 0, 1, 2, ... \tag{1.7}$$

This equation gives the dispersion relation between ω and *k*. Since it is a cubic equation, it has three solutions, namely solutions for *Equatorial Rossby* (ER), *Eastward Inertio-Gravity* (EIG) and *Westward Inertio-Gravity* (WIG) waves. Putting n=0, would give an additional solution, namely *Mixed Rossby Gravity* (MRG) wave. Another special case is the solution obtained when *v*=0 is substituted in equations (1.1)-

(1.3). This solution is called a *Kelvin* wave. It should also be noted that the Kelvin wave solution would be obtained by substituting n=-1 in (1.7)(and hence called a special solution). Figure 1.1 shows the above discussed dispersion curves.

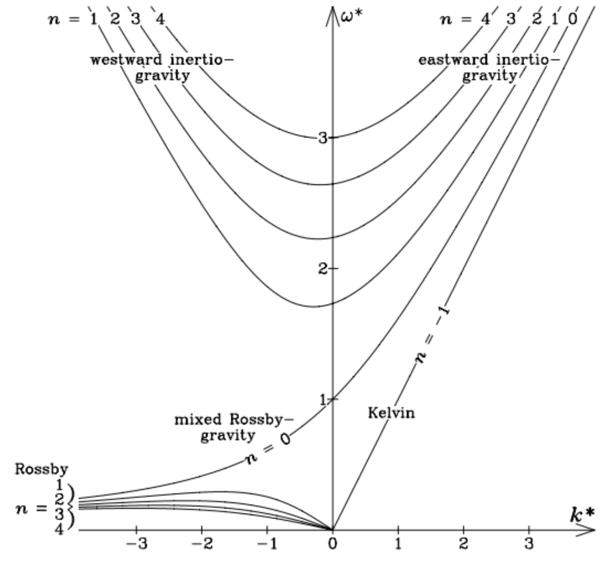

Figure 1.1: Dispersion curves for WIG(n=1,2,3,4), EIG(n=1,2,3,4), ER(n=1,2,3,4), MRG and Kelvin. Note that the dispersion curves are plotted as functions of ω^* and k^* which are non- dimensionalized ω and k. ω^*=$\frac{w}{(\beta\sqrt{gh_e})^{\frac{1}{2}}}$ and k^*=$k(\frac{\sqrt{gh_e}}{\beta})^{\frac{1}{2}}$. Westward propagating waves appear on the left and Eastward propagating waves appear on the right. Note how MRG resembles ER on the left and EIG on the right.(**Source: Kiladis et al [2009]**)

Now, by substituting solutions of *v* from (1.6) to (1.1)- (1.3), we get solutions for *u* and ϕ. this would give us the full horizontal structure of the various wave solutions. It is also important to note that since SWE are a set of linear equations, any linear combination of the wave solutions is also a solution. Equatorial waves are found to exist in the real atmosphere and they approximately follow the theoretical dispersion relations. But the theoretical equatorial waves we dealt with in SWE are different from the real equatorial waves in the atmosphere, because SWE does not take moisture present in the atmosphere and mean states into account or in other words, SWE deals with linear waves.

1.1.2 Equatorial Waves

Equatorial waves are trapped in the equatorial region, which essentially means that their meridional velocity *v* tends to zero at large distances from the equator.

We need four parameters to characterize equatorial waves: meridional mode number *n*, frequency ω, zonal wave number *k* and equivalent depth h_e. We can relate h_e to the phase speed of gravity waves as $c = \sqrt{gh_e}$. h_e is also related to the vertical wavelength of dry waves [Kiladis et al, 2009]. As discussed in the previous section, the theoretical dispersion relation would completely characterize the wave, given *n* and the wave type. This gives rise to two kinds of wave solutions, solutions that are symmetric about the equator and solutions that are anti- symmetric about the equator[*Matsuno*, 1966].

Out of the six specific wave solutions that we considered in the previous subsection, Kelvin, ER, EIG(*n*=1) and WIG(*n*=1) are symmetric about the equator while, MRG, EIG(*n*=0), EIG(*n*=2) and WIG(*n*=2) are anti-symmetric about the equator.

In this study we focus on the effects of backgrounds set by various mean states on the equatorial waves. SWE does not consider the presence of such background states. This way we would be able to see the differences between theoretical convectively coupled equatorial waves (CCEWs) and real CCEWs. We will be considering the backgrounds set by various seasons, El-Nino Southern Oscillation(hereafter ENSO) and Quasi-Biennial Oscillation(hereafter QBO).

1.1.3 El-Nino Southern Oscillation

ENSO is the quasi-periodic variation of winds and sea-surface temperature(SST) over the Eastern Pacific ocean in the tropics. It has been found to mostly affect the tropical and sub-tropical regions. The oscillation goes through a warm phase, a cold phase and neutral phase. The warm phase is called *El-Nino* and the cold phase is called *La-Nina*. *El-Nino* phases usually last several months while *La-Nina* phases usually for 1-2 years.

In this study we will be mainly focusing on the mean states set by the warm and the cold phases of ENSO and its effects on equatorial waves

1.1.4 Quasi-Biennial Oscillation

QBO refers to the quasi-periodic oscillation of the equatorial zonal wind between easterly and westerly phases in the tropical stratosphere. It has a mean time period of about 30 months.

In this study, we will examine the mean states set by the easterly and the westerly phases of QBO and its effect on equatorial waves.

1.2 Data

One of the main data-sets used in the study is the interpolated daily averaged *Outgoing Long-wave Radiation*(hereafter OLR) data, extending from January 1979 to December 2011, obtained from NOAA, Boulder, Colorado, USA, from their Web site at https://www.esrl.noaa.gov/psd/. This data is useful as a proxy for deep tropical convection. 4 times daily zonal wind data-set(u) at 850hPa (hereafter u850), which is part of multi-level wind data, extending from January 1979 to December 2011, obtained from *ERA Interim* is also used in this study. u850 was further averaged to obtain daily averaged zonal wind data for the required years. All the datasets have a horizontal resolution of 2.5^o×2.5^o.

Different phases of ENSO were identified from the NINO-3.4(5N-5S, 170W-120W) index provided by NOAA National Centers for Environmental Information. Using this index, we have identified 10 El-Nino phases and 9 La-Nina phases. Different phases of QBO were identified from the zonal wind index at 30hPa(hereafter u30) provided by *NOAA*(http://www.cpc.ncep.noaa.gov/data/indices/qbo.u30.index). The easterly phase of QBO is identified by easterly zonal winds at 30 hPa exceeding a threshold of -6ms^{-1} in summer and -5ms^{-1} in winter, while westerly phase is identified by westerly zonal winds at 30 hPa exceeding a threshold of $+6ms^{-1}$ in summer and $+5ms^{-1}$ in winter. This gives us 14 easterly phases and 14 westerly phases from 1979 to 2011 in total.

1.3 Wavenumber-Frequency Spectra of OLR and u850

The Space-Time Spectral Analysis(STSA) technique introduced by *Wheeler-Kiladis* [1999](hereafter WK99) was used to isolate zonally propagating convectively coupled equatorial waves. This technique decomposes data that are functions of time and longitude into wavenumber and frequency for eastward and westward propagating waves [WK,1999].

We briefly discuss WK methodology here. Since we are interested in processes with time-periods ranging from few weeks to few months, we will be calculating spectral signatures in the many successive overlapping 96-day segments of the multi-year data-sets. The first three harmonics, time mean and linear trend were removed from the data and the ends of the series are set to zero. Now, FFTs were performed in longitude to calculate Fourier coefficients in wavenumber space at all time and latitude points. Further FFTs were performed in time to obtain wavenumber-frequency spectrum for all latitudes. The average spectral power was then calculated over the entire years for latitudes from 15°N-15°S. Furthermore, this method makes use of an antisymmetric- symmetric decomposition about the equator. To bring out the equatorial wave signal, a background spectrum is defined which is an average of antisymmetric and symmetric power, which is further smoothed by a 1-2-1 filter. The raw spectra are normalized by this background spectrum to obtain the symmetric and antisymmetric wave modes. More details on this method are given in Wheeler-Kiladis 1999.

The WK99 method is a powerful tool to identify CCEWs as it helps to identify finer powers, which are otherwise obscured by the redness of the spectrum. The alignment of the powers along the theoretical dispersion curves(Figure 1.2) validates the results in Matsuno, 1966. The power at wavenumbers 1-3 at about 30-50 days time period shows the presence of Madden-Julian Oscillation(hereafter MJO) which was not predicted by shallow water theory. For Kelvin and ER h_e=50m is the best matching dispersion curve. But this is about an order less than the equivalent depths expected for from theoretical predictions [Kiladis et al,2009]. The likely cause of such shallower equivalent depth is due to the interaction of wave dynamics with convection[Kiladis et al,2009].

The STSA of OLR and u850 was done over seasonally stratified data-sets and for periods corresponding to El-Nino and La-Nina conditions identified using the NINO-3.4 index. Stratification based on different QBO phases were also carried out and the STSA of OLR and u850 was computed. To bring out the difference in forcing of different background states on the equatorial waves, mainly Kelvin, ER (*n=1*), MRG and EIG, we examined the average spectral power corresponding to the wavenumber, frequency and equivalent depth ranges that define each wave mode.

Figure 1.3 shows the anti-symmetric/background power spectra for the 3-month seasons Dec-Feb, Mar-May, Jun-Aug and Sep-Nov(hereafter DJF, MAM, JJA and SON respectively). SON seems to have the highest power in EIG(n=0), and DJF the lowest power at lower wavenumbers. Both MRG and EIG(n=0) between equivalent depths 12m-25m shows significantly more power during SON. So we find that MRG and EIG (n=0) wave modes are relatively more active during SON and least active during DJF despite these two seasons being close to each other.

Figure 1.4 shows the symmetric/background spectra for DJF, MAM, JJA, and SON. MJO is at its strongest during MAM and weakest during JJA and SON. Kelvin wave activity is at its weakest during DJF and strongest during MAM. However ER(n=1) wave activity is not changed significantly by these seasons other than MAM when it shows significant power at wavenumbers well above 5. So we conclude that MJO is significantly stronger during MAM, Kelvin is at its strongest and fastest state during MAM, and ER(n=1) is also prominent at higher wavenumbers during MAM.

Figure 1.5 shows the composite OLR wavenumber-frequency spectra for El-Nino(a

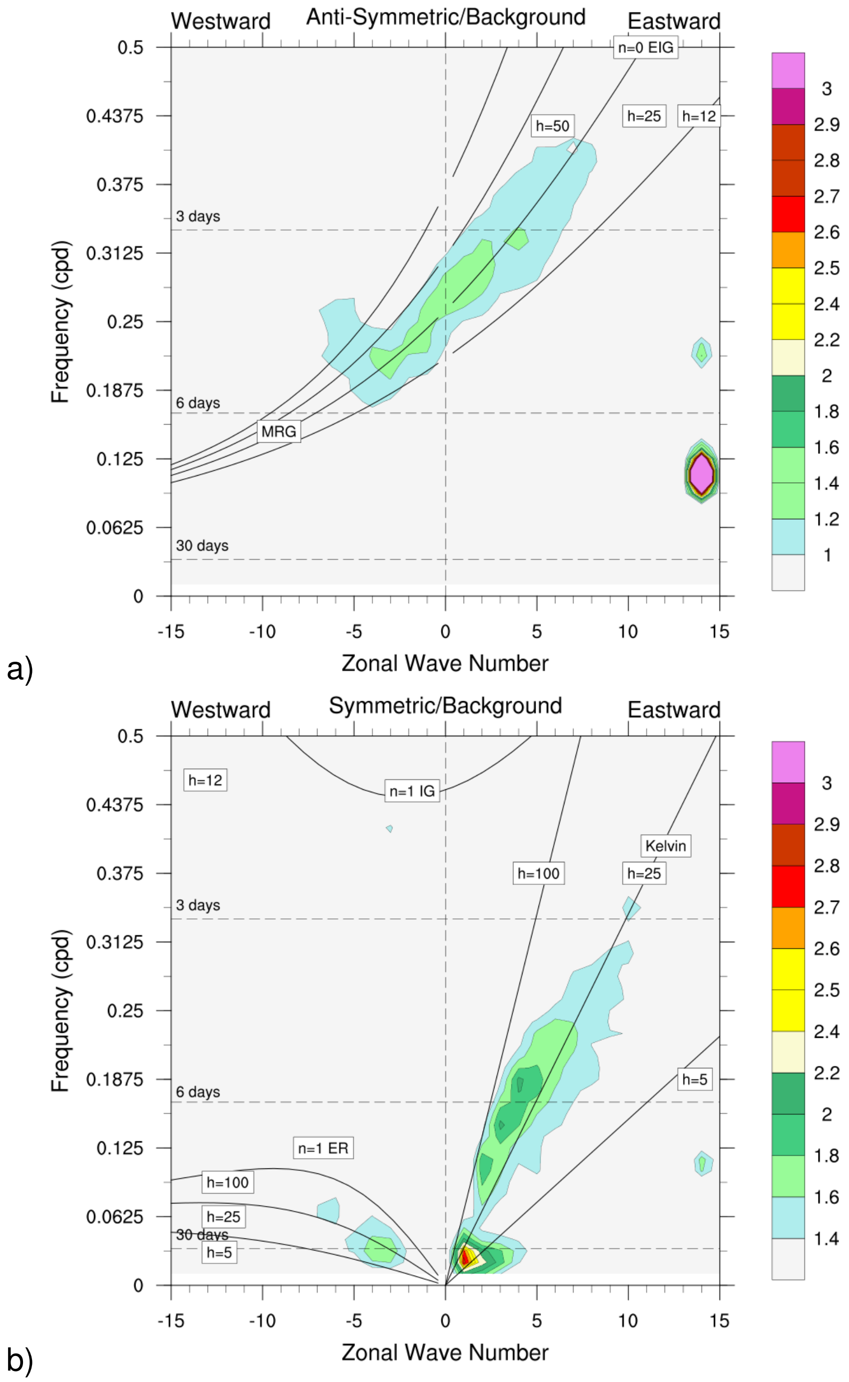

Figure 1.2: :Normalized wavenumber-frequency spectra of OLR for 1979-2011 are shown. a)Anti-symmetric OLR power is shown. Shading begins at 1.0, for which the signal strength is statistically significant. Note the theoretical dispersion curves for MRG and EIG(n=0) superimposed over the spectrum. Each dispersion curve for a wave type represents the theoretical dispersion relation with a specific equivalent depth. Corresponding equivalent depths are labelled. b)Symmetric OLR power is shown. Shading begins at 1.4 for which the signal strength is statistically significant. Theoretical dispersion curves for Kelvin and ER(n=1) are drawn. Corresponding equivalent depths are labelled.

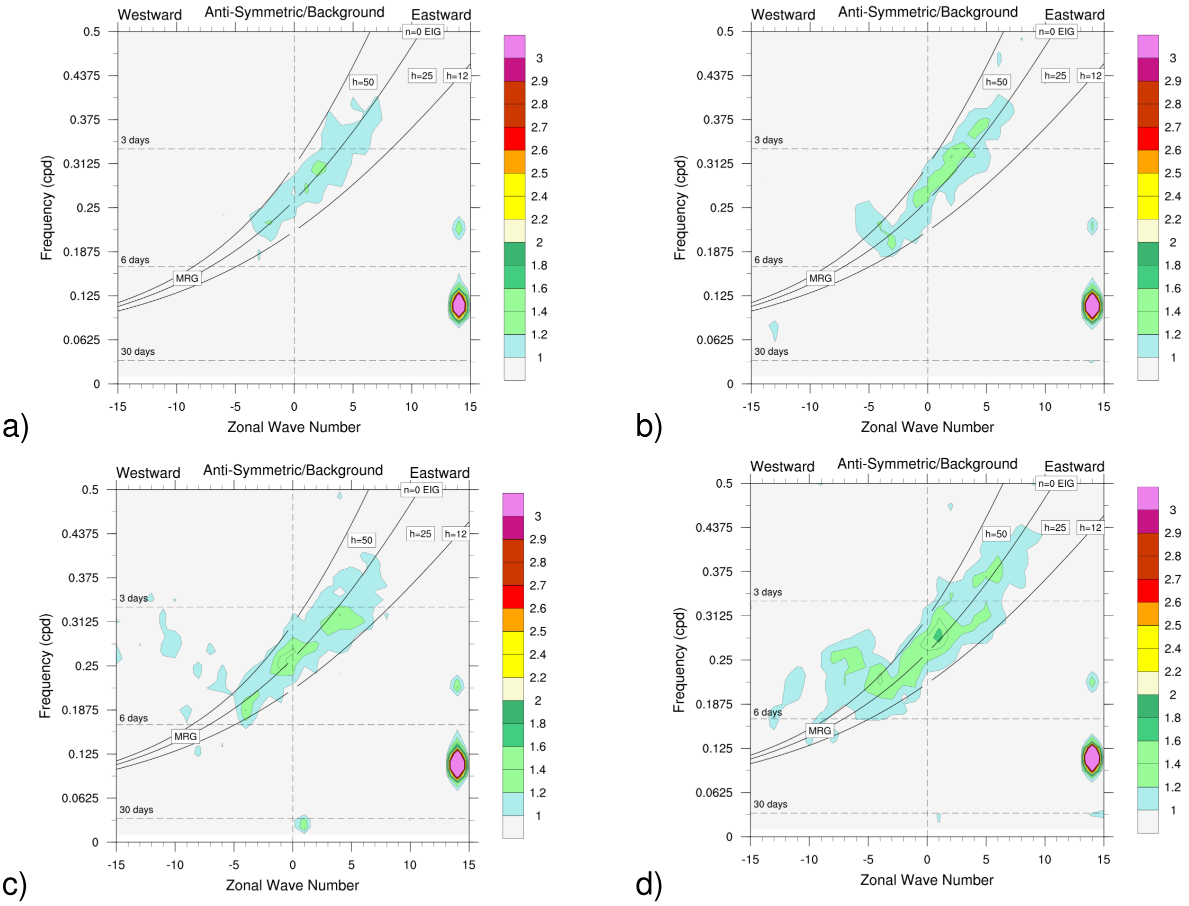

Figure 1.3: Anti-symmetric/Background OLR spectra for 3-month seasons Dec-Feb(a), Mar-May(b), Jun-Aug(c) and Sep-Nov(d) during 1979-2011 taken together and averaged.

and b) and La-Nina(c and d) conditions. Although it looks very similar to Figure 1.2, careful inspection reveals subtle differences.

In the symmetric/background spectrum for El-Nino, there is higher power for Kelvin wave at wavenumber 5 and frequency 0.1875 cpd. Kelvin wave also has significant power at wavenumbers higher than 10 and frequency close to 0.28cpd. In case of ER(n=1) wave there is a shift in the power towards higher wavenumbers close to h_e=5m and h_e=25m during El-Nino. In the anti-symmetric/background spectrum for El-Nino, EIG(n=0) wave has higher power close to wave-number 5 and also at very high frequencies (close to 0.4375cpd) and although MRG wave activity is more concentrated at lower wavenumbers, it is relatively stronger during La-Nina. So El-Nino conditions favor symmetric wave modes while La-Nina conditions favor antisymmetric

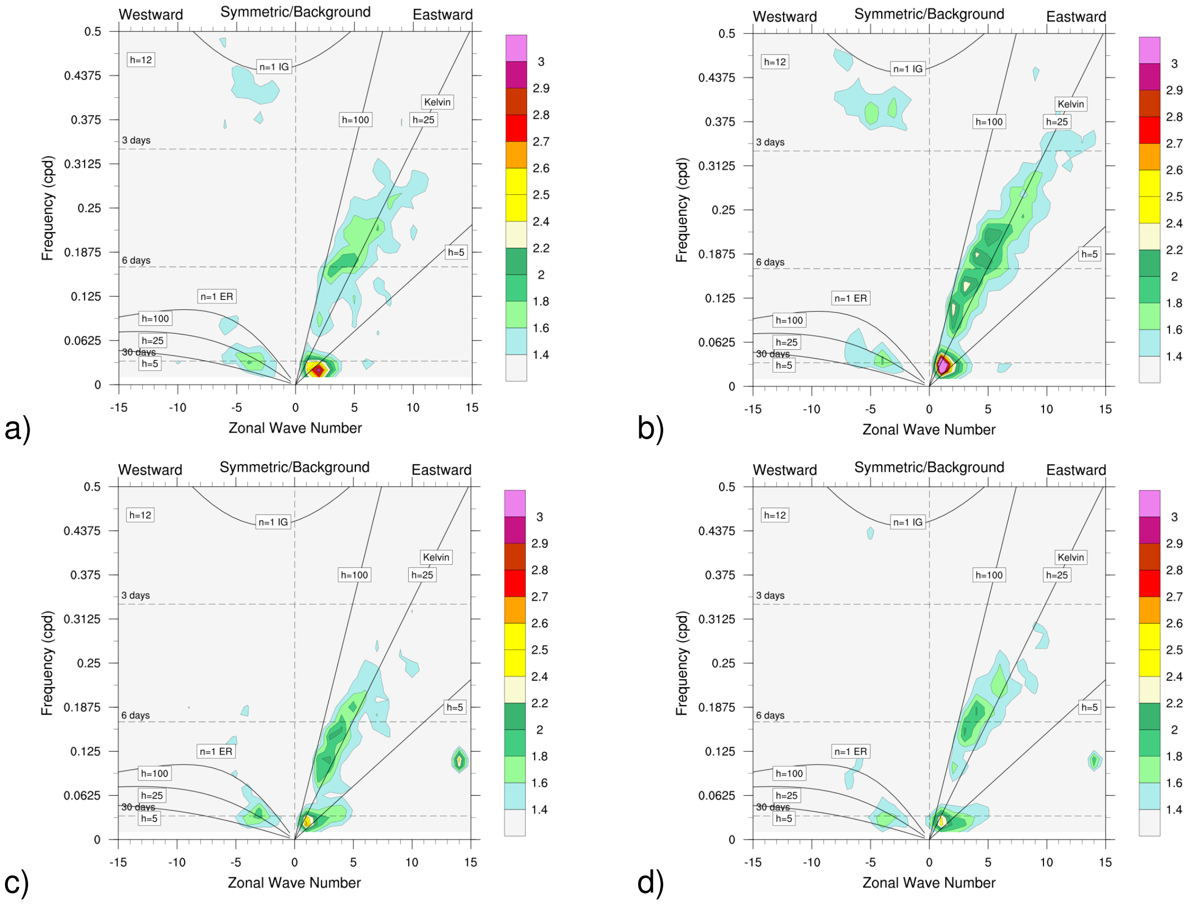

Figure 1.4: Same as Figure 1.3 but shows Symmetric/Background spectra.

wave modes.

During the Easterly phase of QBO (Figure 1.6a and 1.6b), MRG seems to be more active at higher frequencies at wavenumbers beyond -5 while consistently stronger between wavenumber -1 to -5 around and equivalent depth of 25m. But no significant difference seems to be shown by ER(n=1). During the Westerly phase of QBO(Figure 1.6c and 1.6d) however, Kelvin wave shows prominence also at higher frequencies and wavenumber but is restricted mostly between equivalent depths 25m-100m. Kelvin wave also shows higher power close to an equivalent depth of 100m. MJO also seems to be propagating with higher wavenumbers during the Westerly phase of QBO. Table 1.1 summarizes the results obtained from STSA of OLR during different background conditions.

In the normalized wavenumber-frequency spectra of u850(Figure 1.7), MJO seems

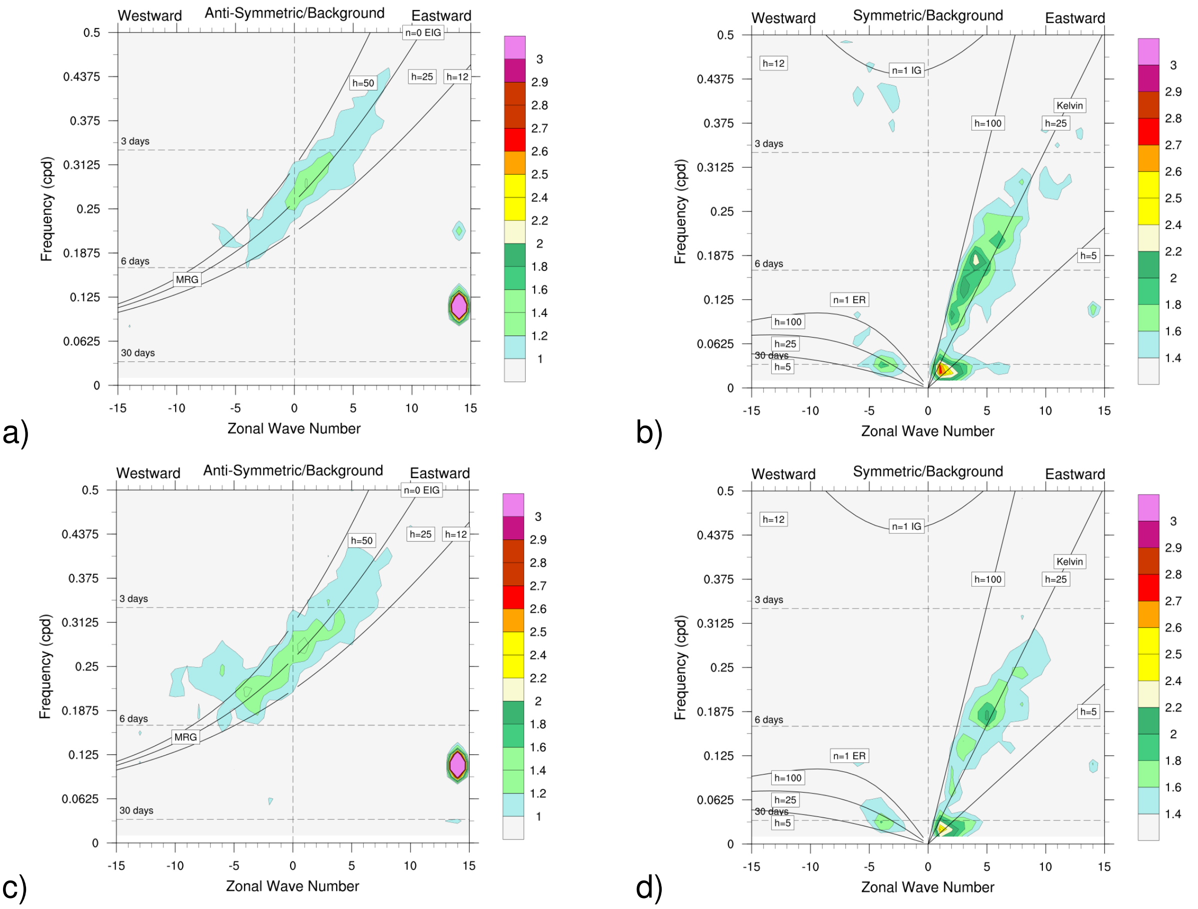

Figure 1.5: Same as Figure 1.3 but for El-Nino(a and b) and La-Nina(c and d) events respectively during 1979-2011 taken together and averaged.

Wave Type	Average	DFJ	MAM	JJA	SON	El-Nino	La-Nina	QBO-E	QBO-W
Kelvin	1.49	1.45	1.59	1.38	1.37	1.54	1.48	1.53	1.47
ER	1.29	1.29	1.27	1.27	1.28	1.28	1.28	1.28	1.28
MRG	1.03	1.01	1.05	1.06	1.08	1.01	1.12	1.08	1.07

Table 1.1: The area averaged powers(W/m^2) for different CCEWs in the WK spectra of OLR are shown for various periods. The power is averaged over an area that lies below a frequency of 0.3cpd, between wavenumbers -10 and -1 (for ER and MRG) and (1 and 10 for Kelvin) and equivalent depths 5m-100m (for Kelvin and ER) and 12m-50m(for MRG).

to be concentrated only at wavenumbers 1 and 2 unlike in OLR. While ER(n=1) signal is completely absent the signal for 5-day Rossby-Hauritz wave is evident in u850. Since this is not a convectively coupled equatorial wave, we are not including this in our present study. However, it is reasonable to approximate the 5-day Rossby-Hauritz wave as ER with an approximate equivalent depth of 1000m and also this wave mode

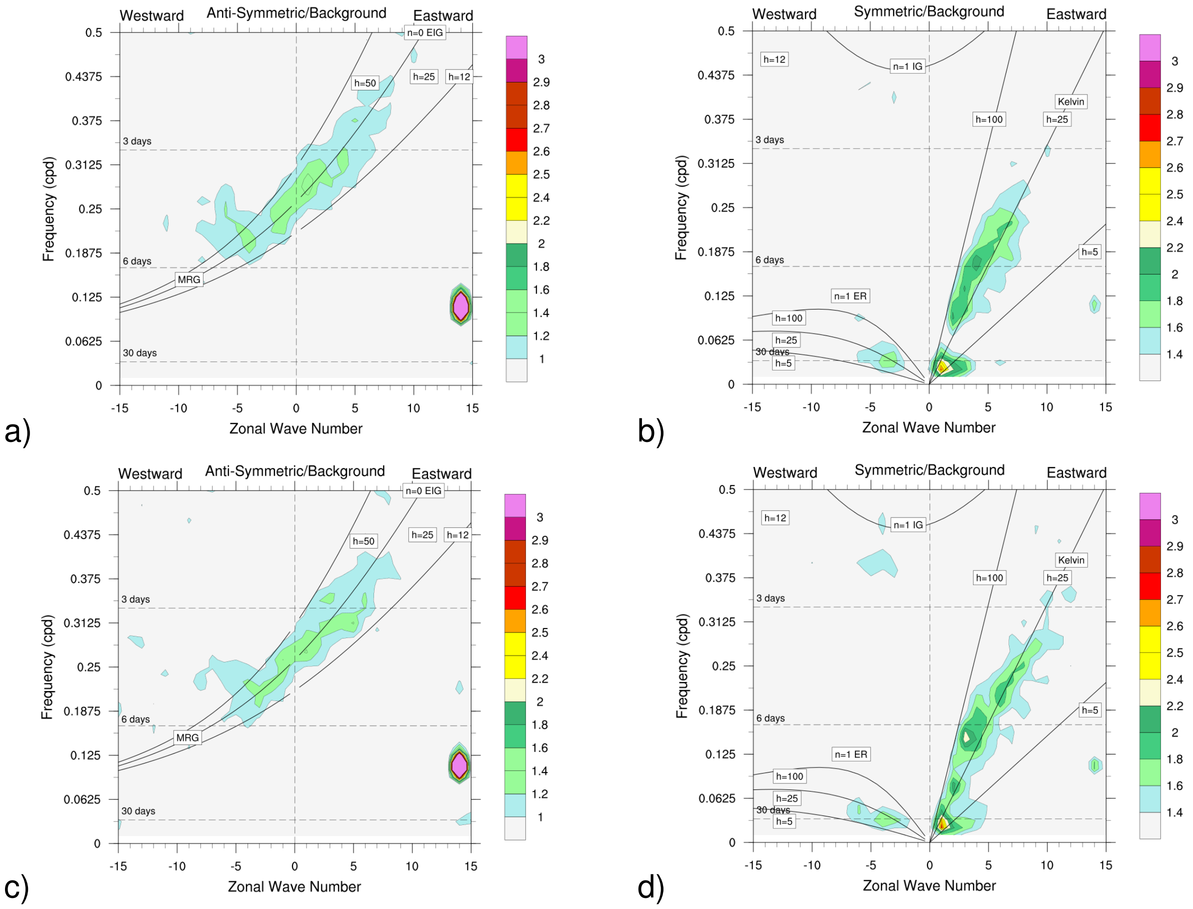

Figure 1.6: OLR wavenumber-frequency spectra during the Easterly phase of QBO(a and b) and Westerly phase of QBO(c and d) respectively during 1979-2011 taken together and averaged.

is found to have an association with convection[King et al, 2015]. Kelvin wave has a strong signal the symmetric spectra of u850 but is restricted to equivalent depths from 25m-100m. However Kelvin wave does not have a significant power below a 0.093cpd frequency other than that of the MJO. In the anti-symmetric/background spectra EIG(n=0) is found to dominate in the high frequency region while westward moving MRG does not have significant spectral power.

Figure 1.8 shows the seasonal variation of symmetric equatorial waves. Kelvin wave has a wavenumber-frequency spectra in u850 that is very similar to the OLR spectra. Kelvin wave shows the highest power during MAM similar to OLR and is restricted between equivalent depths of 25m-100m. But unlike in OLR spectra, MJO has higher spectral power in u850 spectra during all four seasons. ER(n=1) wave

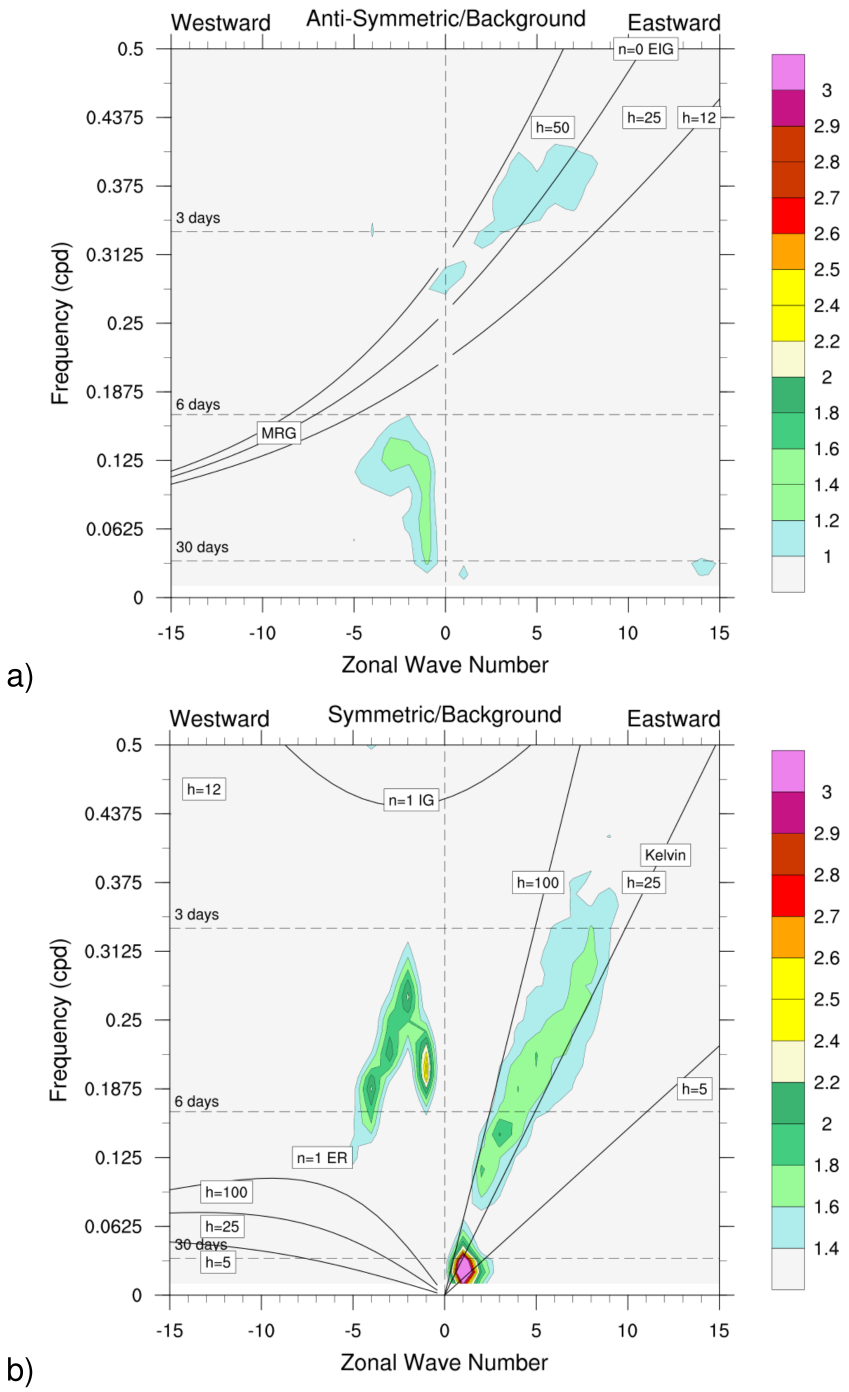

Figure 1.7: Normalized wavenumber-frequency spectra of u850 for 1979-2011. Specifications are the same to those mentioned in Figure

activity is not evident in u850 power spectra. However, the 5-day Rossby-Hauritz wave is at its strongest during MAM, which verifies the results in [King et al, 2015].

Figure 1.9 shows WK spectra of u850 for El-Nino and La-Nina events. MJO and Kelvin wave are relatively stronger during El-Nino. ER(n=1) wave activity again is not

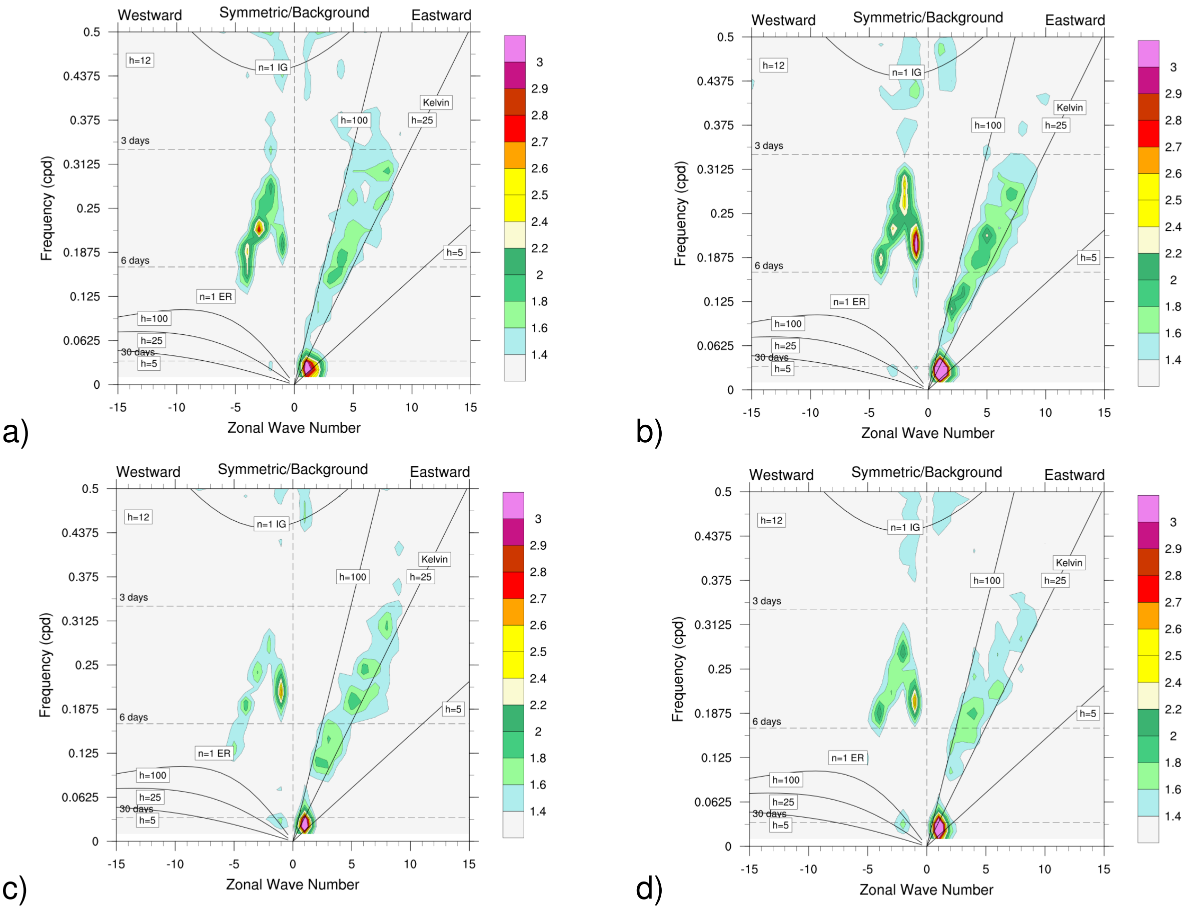

Figure 1.8: Symmetric/background spectra of u850 over a)DJF, b)MAM, c)JJA and d)SON.

evident in u850 power spectra. Although EIG(n=0) wave activity is slightly more evident in u850 power spectra during ENSO events, MRG wave is still not significantly strong.

Figure 1.10 shows the normalized wavenumber-frequency spectra of u850 during easterly and westerly phases of QBO. Kelvin wave has more power during the easterly phase of QBO, than during the westerly phase of QBO. Table 1.2 summarizes the results of u850 power spectra under different background conditions

The area-averaged powers of the spectra of u850 are shown in Table 1.2. Average power of Kelvin wave follows a trend similar to the one in Table 1.1, but ER and MRG don't.

Comparing Figures 1.2 and 1.7, we can infer that Kelvin wave has a strong power in both OLR and u850 and that the majority of the power is restricted between 25m-100m equivalent depths. In OLR spectra Kelvin wave is not very prominent in higher

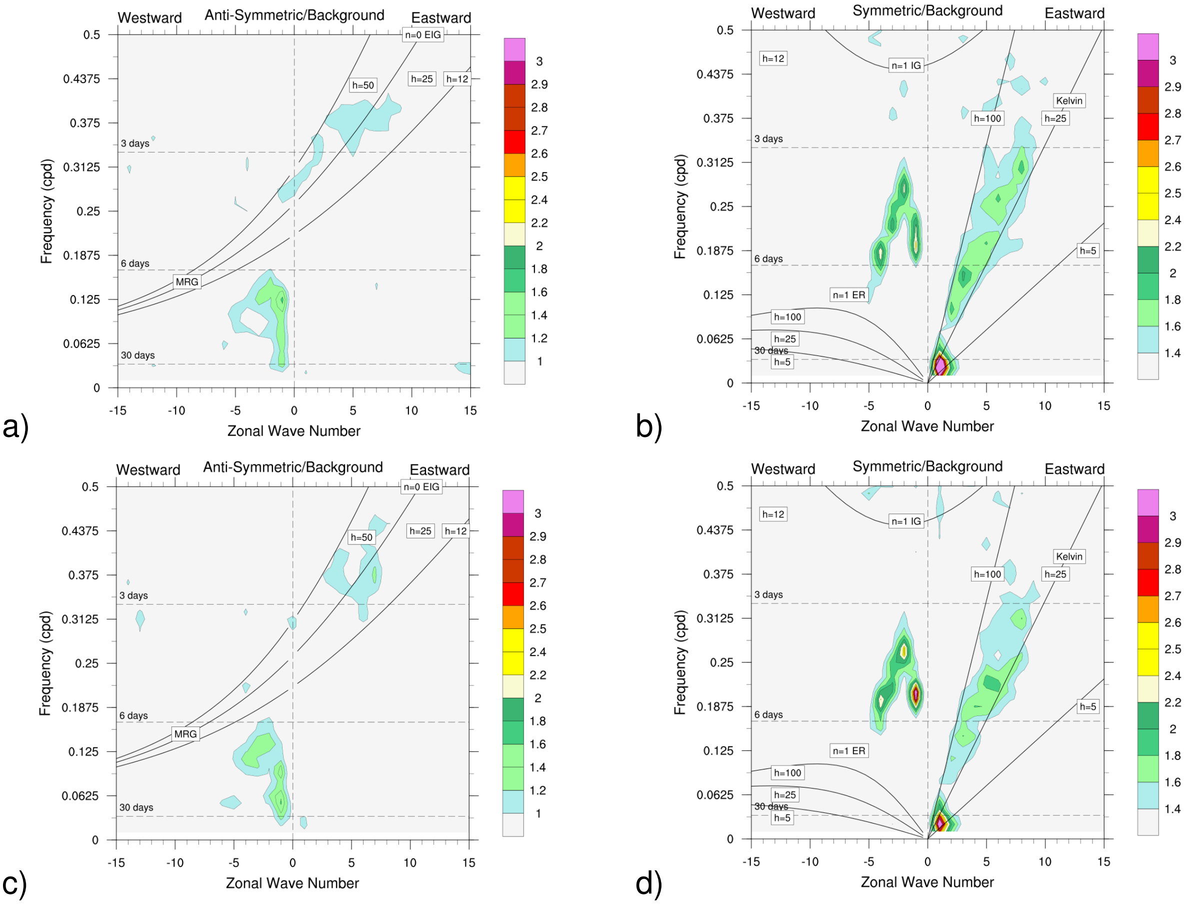

Figure 1.9: Normalized wavenumber-frequency spectra of u850 during El-Nino(a and b) and La-Nina(c and d) events respectively over 1979-2011 taken together and averaged.

Wave Type	Average	DFJ	MAM	JJA	SON	El-Nino	La-Nina	QBO-E	QBO-W
Kelvin	1.55	1.50	1.61	1.49	1.48	1.55	1.48	1.52	1.48
ER	1.11	1.12	1.07	1.07	1.10	1.07	1.07	1.08	1.08
MRG	0.79	0.81	0.85	0.80	0.81	0.84	0.80	0.84	0.83

Table 1.2: The area averaged powers(W/m^2) for different CCEWs in the WK spectra of u850 are shown for various periods. The power is averaged over an area that lies below a frequency of 0.3cpd, between wavenumbers -10 and -1 (for ER and MRG) and (1 and 10 for Kelvin) and equivalent depths 5m-100m (for Kelvin and ER) and 12m-50m(for MRG)

wavenumber and frequency realm and in U850 spectra Kelvin wave is not very strong in lower wavenumber-frequency region. This implies that Kelvin wave is capable of propagating zonally with a wide range of wavelengths and periods. However the activity of Kelvin wave is strongly dependant on the phases of ENSO, which is evident from the difference in powers of Kelvin wave during El-Nino and La-Nina in both OLR and

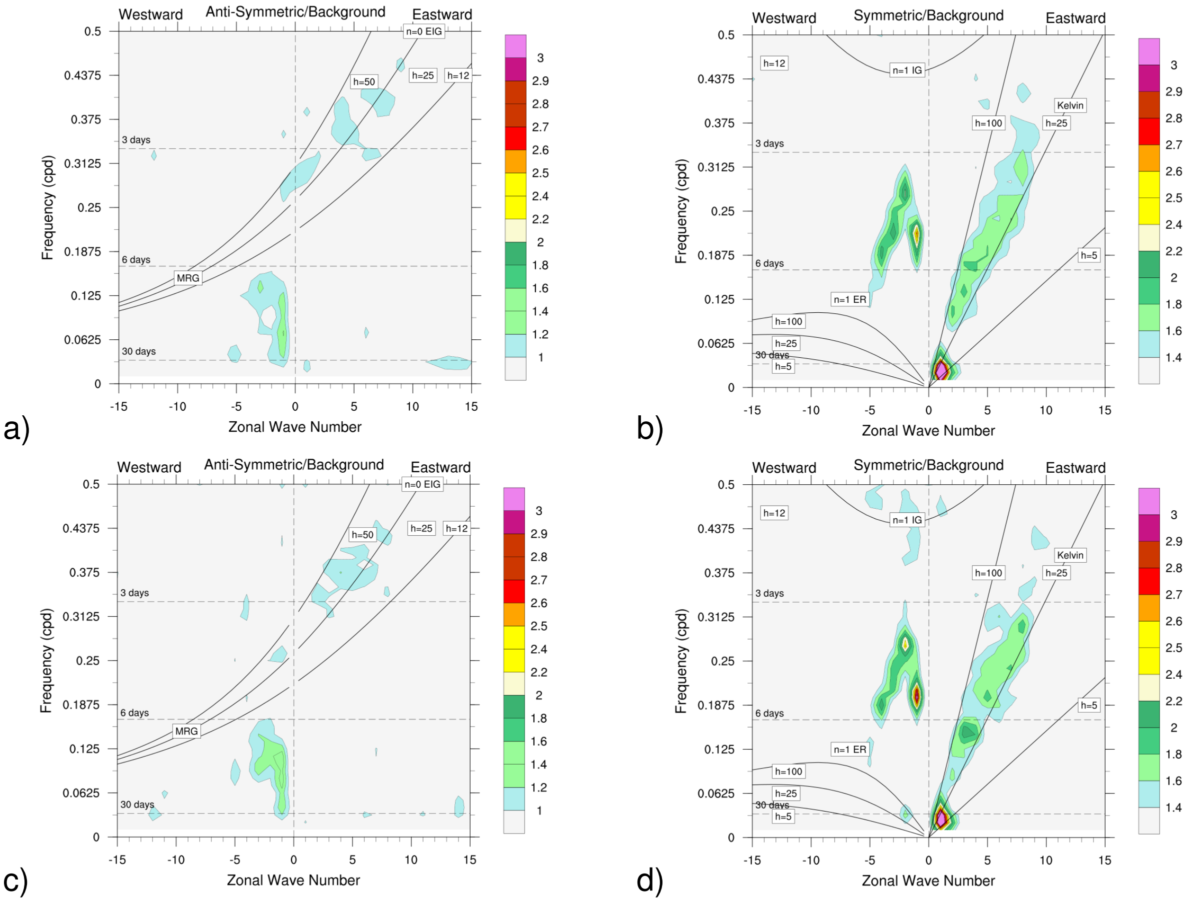

Figure 1.10: Same as Figure 1.9 but during a)Easterly and b)Westerly phases of QBO

u850. The signals of ER and MRG are not very strong in the spectra of u850.

Although power spectra of OLR and u850 does give us information about CCEWs dependence on background conditions, they do not tell us much about coherent signatures (if any) in OLR and u850 spectra. So we move on to analyzing the coherence-squared spectra in the next section.

1.4 Coherence-squared spectra

Space time coherence-squared spectra are computed using two-dimensional complex Fourier transforms. We will briefly discuss the methodology here. The discrete space-time Fourier transforms of two fields (OLR and U850 in this case) defined at *M* equally spaced points in space and *N* equally spaced points in time are as follows:

$$F_1(w,k) = \frac{1}{N}\sum_{n=1}^{N}\frac{1}{M}\sum_{m=1}^{M} f_1(t_n, x_m) exp[-i(wt_n\text{-}kx_m)] \tag{1.8}$$

$$F_2(w,k) = \frac{1}{N}\sum_{n=1}^{N}\frac{1}{M}\sum_{m=1}^{M} f_2(t_n, x_m) exp[-i(wt_n\text{-}kx_m)] \tag{1.9}$$

The powers E_{11} and E_{22} and cross-power E_{12} are then defined as:

$$E_{11} = {F_1}^{*}F_1 \tag{1.10}$$

$$E_{22} = {F_2}^{*}F_2 \tag{1.11}$$

$$E_{12} = {F_1}^{*}F_2 = P_{12}(w,k) + iQ_{12}(w,k) \tag{1.12}$$

where, the quantity super scripted with * is the complex conjugate. P_{12}(co-spectrum) and Q_{12}(quadrature spectrum) are the real and imaginary parts of the cross-power spectrum. Cross-power spectrum is generally complex in nature unlike power spectrum which is always real. Cross-power spectrum contains information about the magnitude and the phase relationship between the two quantities. The standard way of expressing the magnitude of cross-power spectrum is as follows:

$$|\gamma_{1,2}(w,k)|^2 = \frac{|E_{12}|^2}{E_{11}E_{22}} \tag{1.13}$$

where γ_{12} is called the coherence-squared spectrum which is like a squared correlation coefficient, which is bounded between 0 and 1. More details on coherence squared spectrum can be found in Hendon and Wheeler, 2008.

Figure 1.11 shows the coherence-squared spectra and the phase lag relation of OLR with u850. The most striking feature of this is the coherence maxima for MJO which has coherence-squared value close to 0.6. Also note the coherence in ER(n=1) (symmetric) and MRG (anti-symmetric), although the powers of ER(n=1) and MRG in the individual power spectra of u850 were relatively insignificant. The 5-day Rossby Hauritz wave also seems to be statistically significant(at k=-1, ω=0.2). The coherence of OLR with u850 is fairly strong in Kelvin wave also and it is specifically stronger between equivalent depths of 25m-100m similar to the powers of Kelvin wave in Figures 1.3 and 1.8. Coherence-squared values up to 0.3 is observed for Kelvin waves. The vectors in Figure 1.11 indicate the phase-lag relation of OLR with u850. By this, we learn that OLR lags u850 by one-eighth of a cycle in MJO. For Kelvin waves, OLR lags u850 by about one-eighth to one-fourth of a cycle in low wave wavenumbers and OLR and u850 are completely out of phase in high wavenumbers and frequencies. On the other hand, OLR leads u850 by about one-fourth of a cycle for Rossby waves from wavenumber -2 and beyond while OLR lags u850 at wavenumber -1. Also it is worth noting that OLR and u850 are completely out of phase with each other for the westward mode of MRG while while in EIG(n=0), OLR lags u850 by one-eighth of a cycle in equivalent depths less than 25m for wavenumbers 5 and above. Observations in coherence-squared spectra of OLR with u850 are consistent with the results in Hendon-Wheeler, 2008.

The coherence-squared spectra of OLR with u850 during the seasons DJF, MAM, JJA and SON are shown in Figure 1.12. It further validates our results from the seasonal power spectral analysis of OLR(Figures 1.5 and 1.6) and u850(Figure 1.10). Kelvin wave is most active during MAM and the least active during JJA and SON. Although ER did not show any significant variation in power in OLR, the coherence of OLR with u850 for ER is the strongest during SON and the weakest during MAM. Coherence-squared spectral analysis also confirms the presence of strong MRG during SON, which was also observed from the OLR spectrum. The enhanced coherence of OLR with u850 for the 5-day Rossby-Hauritz wave are consistent with the results in King et al,2015.

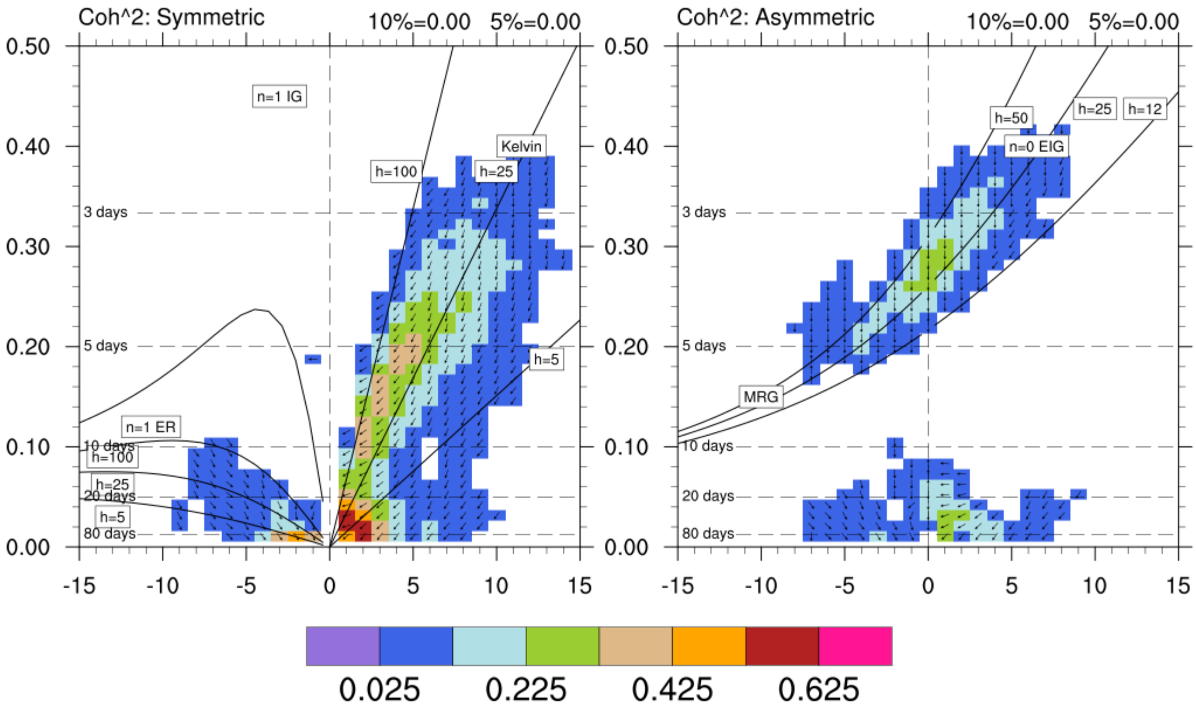

Figure 1.11: Coherence-squared spectra of OLR with u850 for a period of 1979-2011. The vectors indicate the phase-lag between OLR and zonal wind. Contour interval is 0.1 and the contours start from 0.025. Vectors pointing directly up indicate zero phase lag and directly down means that OLR is completely out of phase with zonal wind. Rightward vector means that OLR leads u850 by one-fourth of a cycle and leftward vector means OLR lags u850 by one-fourth of a cycle The equivalent depths are kept the same.

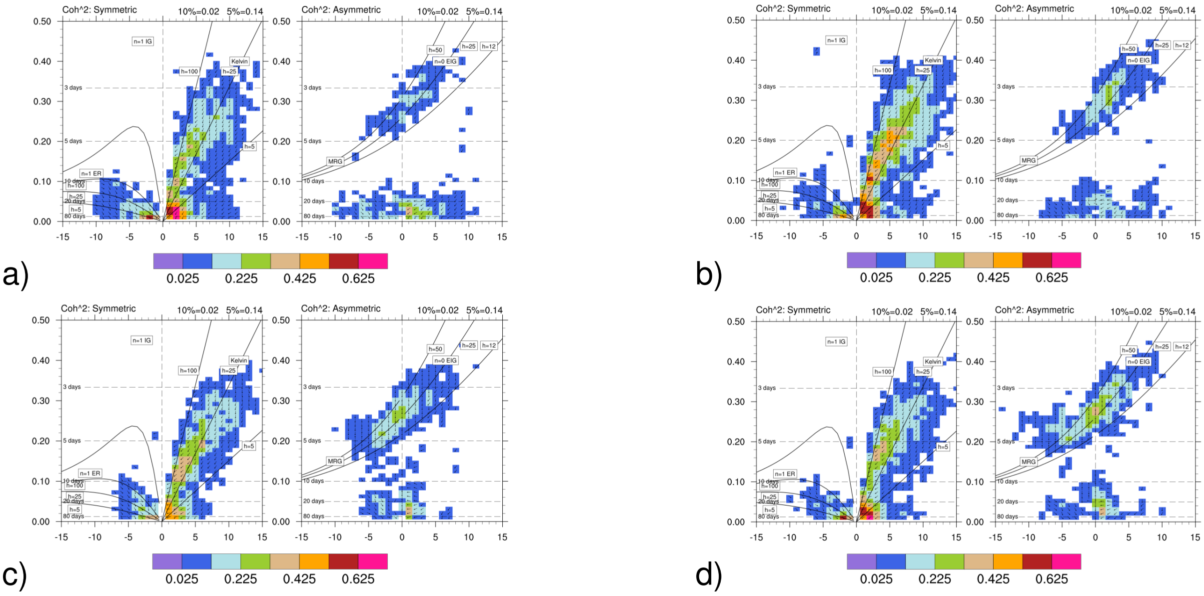

a)

b)

c)

d)

Figure 1.12: Coherence squared spectra of OLR with u850 during the 3-month seasons: a) DJF, b) MAM, c) JJA, d) SON, during 1979-2011.

The major feature of coherence-squared spectra of OLR with u850 during El-Nino and La-Nina(Figure 1.13) is the difference in coherence in MJO and Kelvin between the two extreme backgrounds, which was expected as we did observe similar patterns in Figures 1.4 and 1.9. Rossby waves have a higher coherence, with coherence-squared values up to 0.4 during El-Nino. But MRG and EIG(n=0) waves are more coherent in OLR and u850 during La-Nina. These observations confirm that El-Nino favors symmetric wave modes, while La-Nina favors antisymmetric wave modes. The phase-lag relation between OLR and u850 however, do not change significantly between the two extreme phases of ENSO.

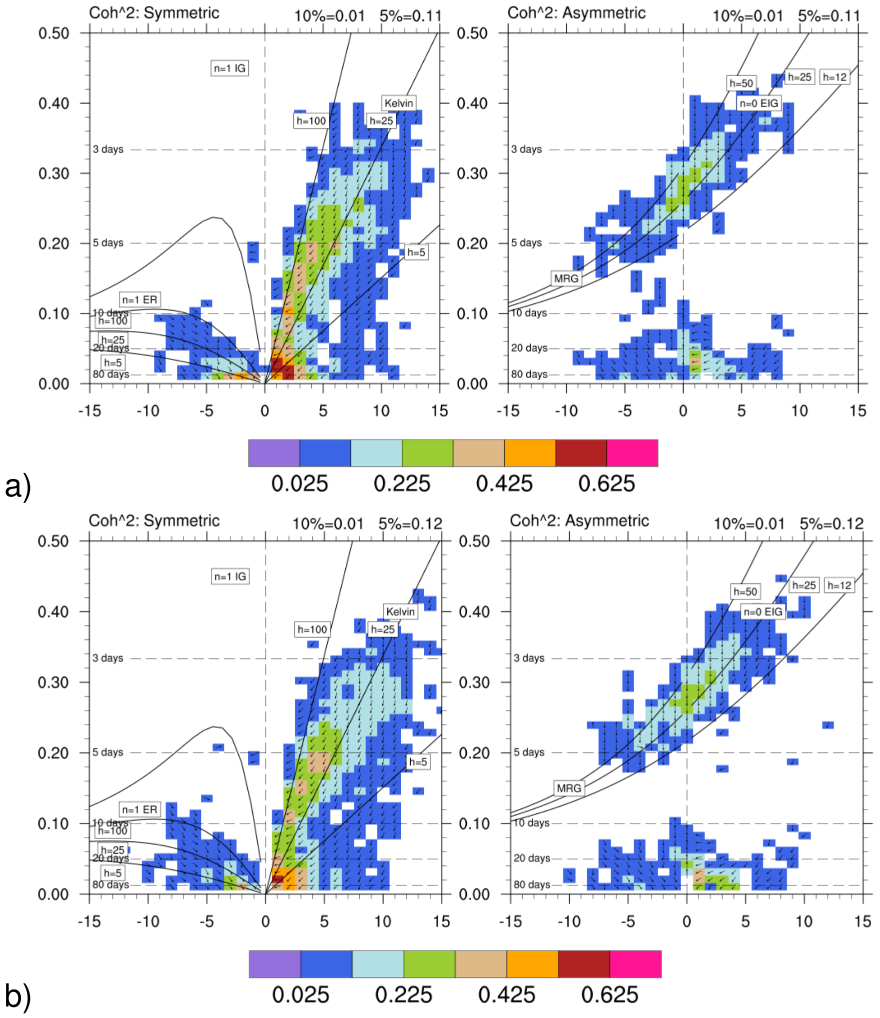

Figure 1.13: Same as Figure 1.11 but for El-Nino(top) and La-Nina(bottom) events.

Figure 1.14 shows the coherence-squared spectra of OLR with u850, during the easterly and westerly phases of QBO. It does not suggest any clear effect of the easterly and westerly phases of QBO on equatorial waves. Table 1.3 summarizes the results of this section.

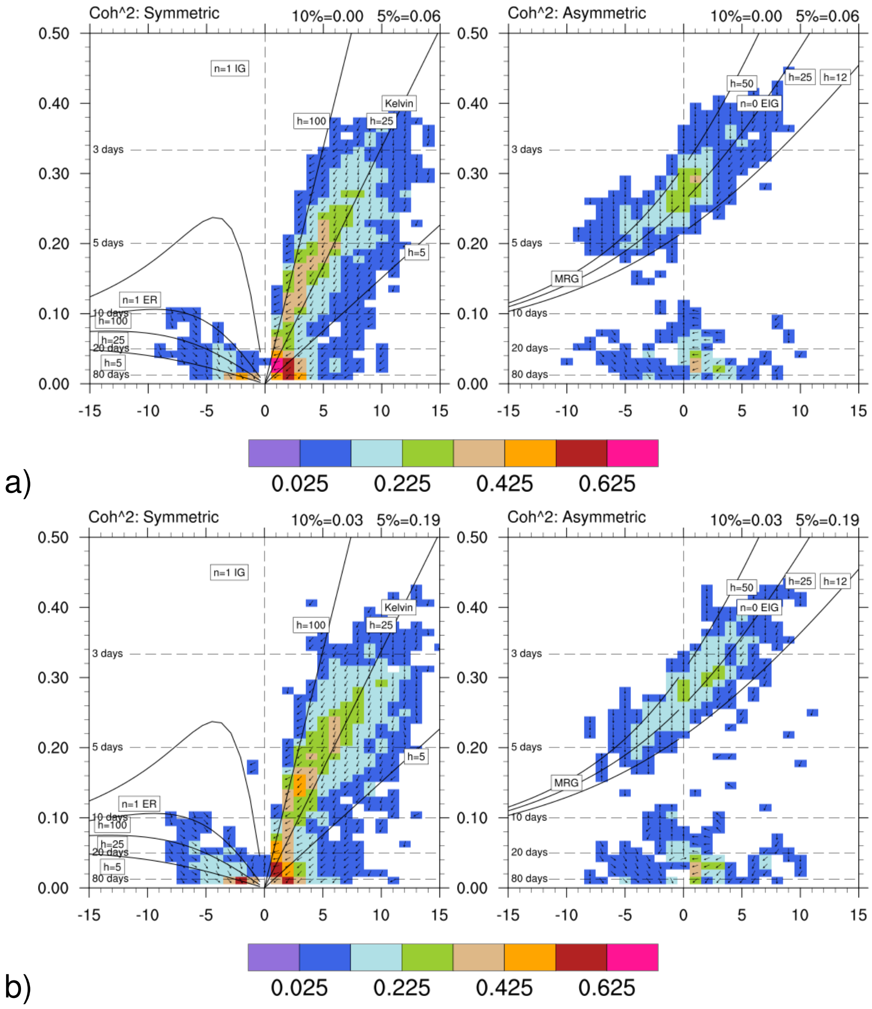

Figure 1.14: Coherence-squared spectra of OLR with u850 during the easterly(a) and westerly(b) phases of QBO.

Wave Type	Average	DFJ	MAM	JJA	SON	El-Nino	La-Nina	QBO-E	QBO-W
Kelvin	0.017	0.25	0.026	0.052	0.026	0.017	0.028	0.023	0.026
ER	0.220	0.242	0.192	0.234	0.273	0.225	0.223	0.214	0.221
MRG	0.022	0.020	0.021	0.023	0.021	0.020	0.022	0.025	0.020

Table 1.3: The area-averaged coherence of OLR with u850 for different CCEWs are shown for various periods. The power is averaged over an area that lies below a frequency of 0.3cpd, between wavenumbers -10 and -1 (for ER and MRG) and (1 and 10 for Kelvin) and equivalent depths 5m-100m (for Kelvin and ER) and 12m-50m(for MRG)

1.5 Distribution of mean variance of OLR to geographically locate CCEWs.

In addition to the analysis done in the previous sections to understand the shift in spectral power, we explore whether the geographically active locations of equatorial waves are affected by the change in background conditions. In order to do this, we filter the OLR data for various wave modes using their wavenumber, frequency and equivalent depth ranges. The variance of these wave-filtered OLR data was computed and plotted to locate the active zones of Kelvin, ER (n=1), westward propagating mode of MRG (WMRG) and EIG (n=0), which is shown in figure 1.15.

According to figure 1.15, Kelvin wave is found to be more prominent over the Indian Ocean and over the entire Pacific Ocean. Rossby waves are more active in the Western Pacific Ocean while MRG is active over the entire Pacific. Although the presence of EIG is significant over the Pacific, it is not as strong as the other wave modes. Figures 1.16, 1.17 and 1.18 show the wavenumber-frequency filtered variance of OLR for the seasonally stratified, ENSO stratified and QBO stratified cases respectively.

Figure 1.16 shows the wavenumber-frequency filtered variance of OLR for various 3-months seasons. As expected, we can see that Kelvin wave has the most power during MAM, but more interestingly, Kelvin wave activity extends beyond the Indo-Pacific region and during MAM it gets powerful almost over the entire equatorial region. Although ER did not show any significant variation in power, geographically it does shift its active zones from season to season. ER is more active in the Southern hemisphere during DJF and MAM, while it is more prominent in the Northern hemisphere during JJA and SON. Same is the case for MRG. This shows that the westward propagating waves are more active in the Southern hemisphere during DJF and MAM, while they are more prominent in the Northern hemisphere during JJA and SON. This feature of ER interestingly matches with the probable duration of tropical cyclone genesis in the Northern and Southern hemispheres respectively(Tropical cyclones occur

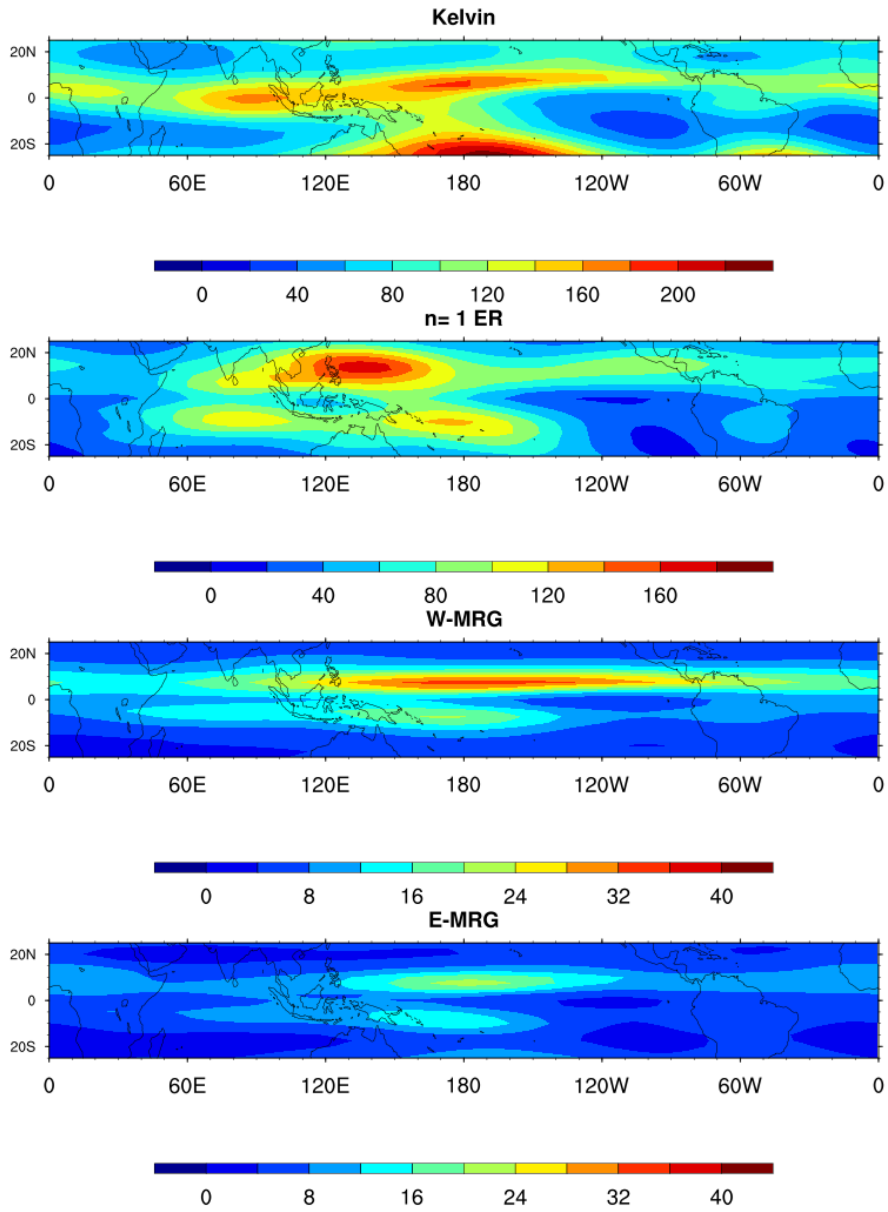

Figure 1.15: Mean variance of OLR for a period 1979-2011 is shown. E-MRG is EIG(n=0). All other waves retain the same name.

from June-November in the Northern hemisphere and November-April in the Southern hemisphere)[https://www.metoffice.gov.uk/weather/tropicalcyclone/facts].

Figure 1.17 validates our observation from Figure 1.2. Kelvin and ER waves(symmetric) are stronger during El-Nino while MRG and EIG(anti-symmetric) are stronger during La-Nina. It is also fascinating to note that the westward propagating waves namely ER and MRG have slightly shifted their respective active zones westward during La-Nina relative to their positions during El-Nino. The shift is not significant for ER wave but it is quite apparent in MRG wave.

There is no relative shift in the active zones of CCEWs between the easterly and westerly phases of QBO. MRG and EIG also are pretty much unchanged between the different phases of QBO.

1.6 Conclusions

Following are the conclusions from this study: 1) The symmetric wave modes are favoured during El-Nino while anti-symmetric wave modes are more prominent during La-Nina. 2) Kelvin wave and ER (n=1) wave have relatively higher spectral power in both OLR and u850 during MAM, while MRG is stronger during SON. 3) The different phases of QBO do not have a consistent influence in the lower troposphere. 4) Kelvin wave is the most sensitive to background conditions. 5) The shift in the active zones of ER during different seasons closely follows the shift in locations of tropical cyclone genesis. 6) The regions of activity of westward propagating wave modes, namely ER and MRG, shift westward during La-Nina, compared to their active zones during El-Nino.

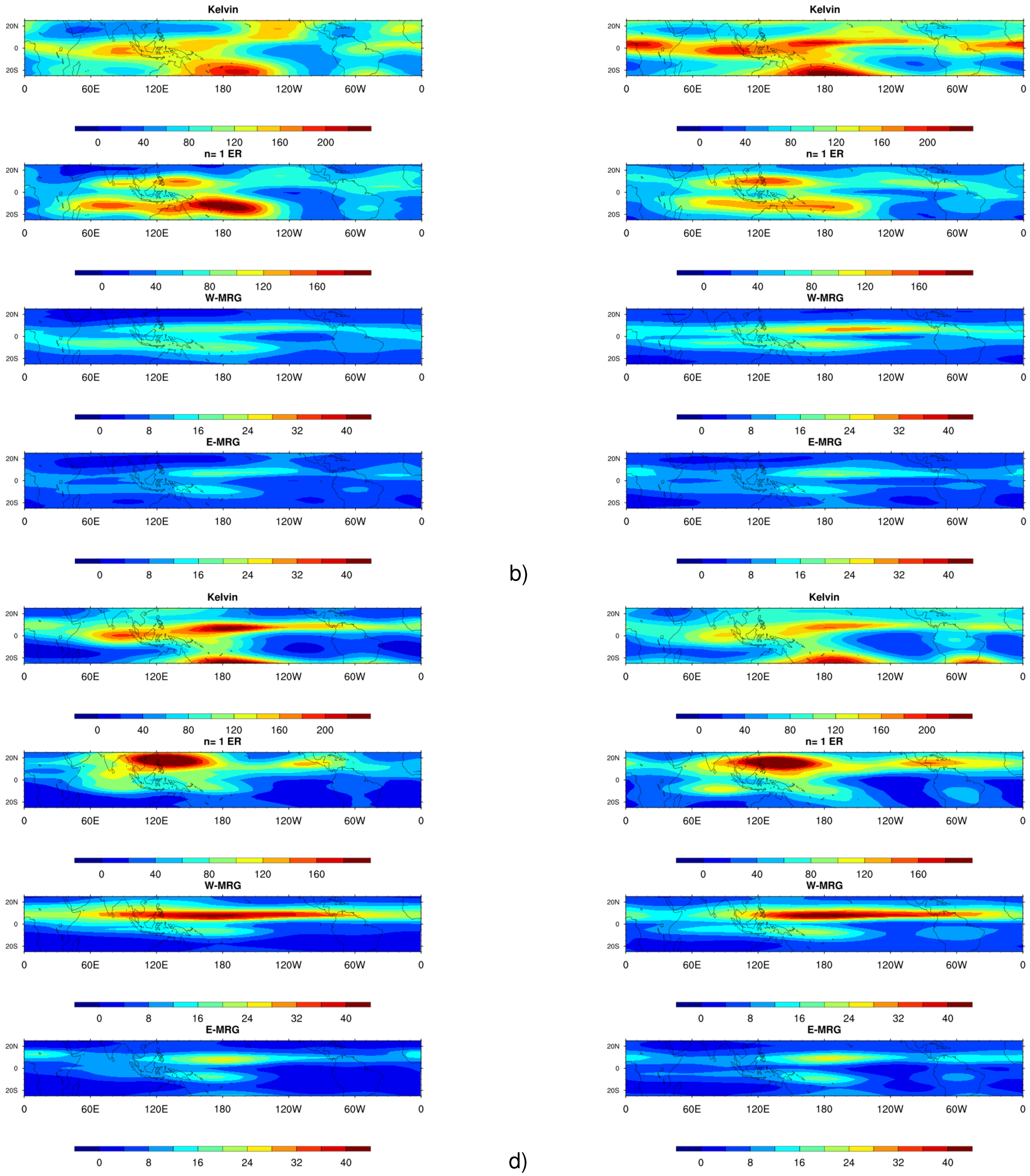

Figure 1.16: Mean variance of OLR during 3-month seasons a)DJF, b)MAM, c)JJA, d)SON for a period 1979-2011 is shown. E-MRG is EIG(n=0). All other waves retain the same name.

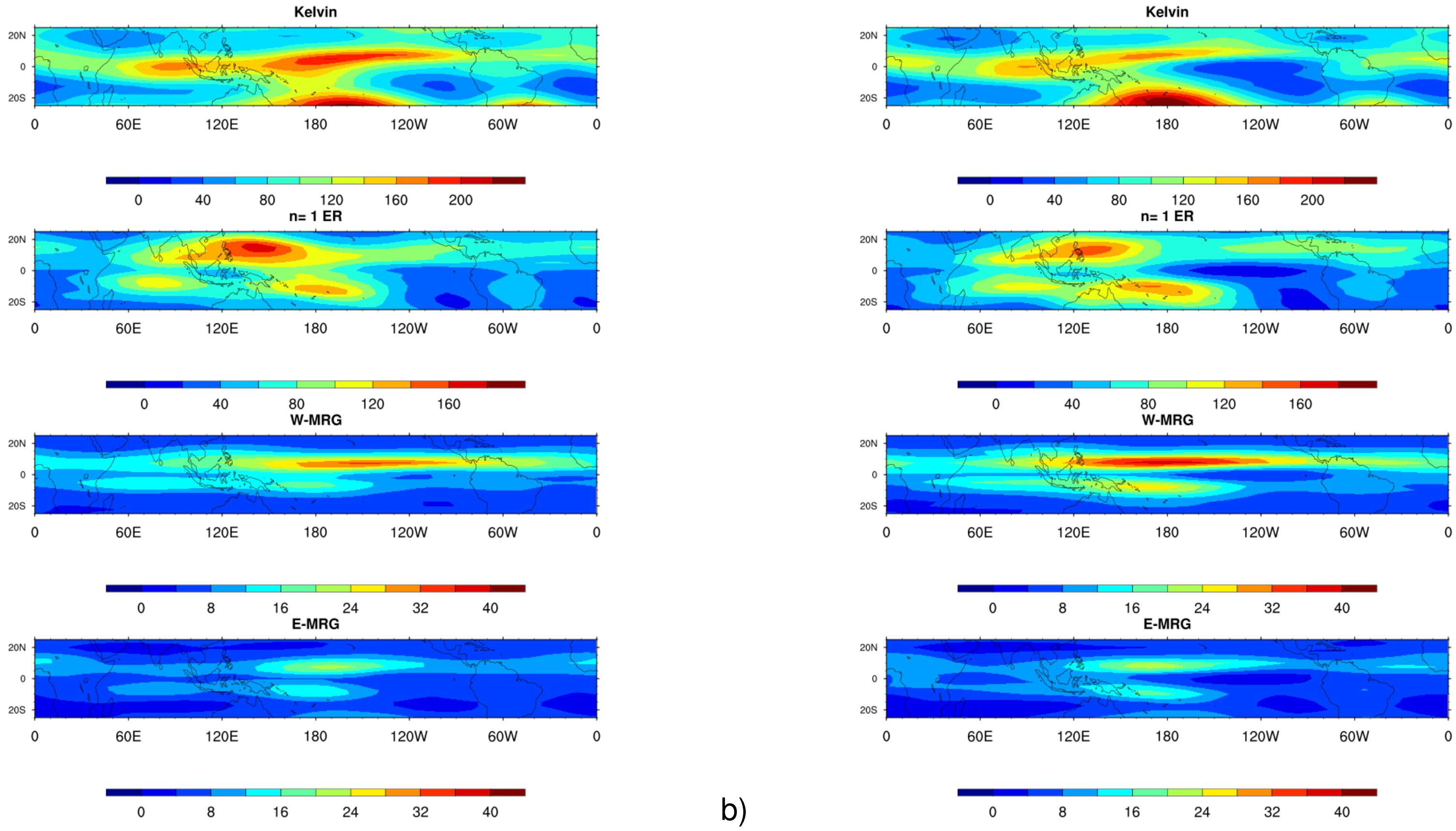

Kelvin

n= 1 ER

W-MRG

E-MRG

b)

Figure 1.17: Mean variance of OLR during a)El-Nino and b)La-Nina for a period 1979-2011 is shown. E-MRG is EIG(n=0). All other waves retain the same name.

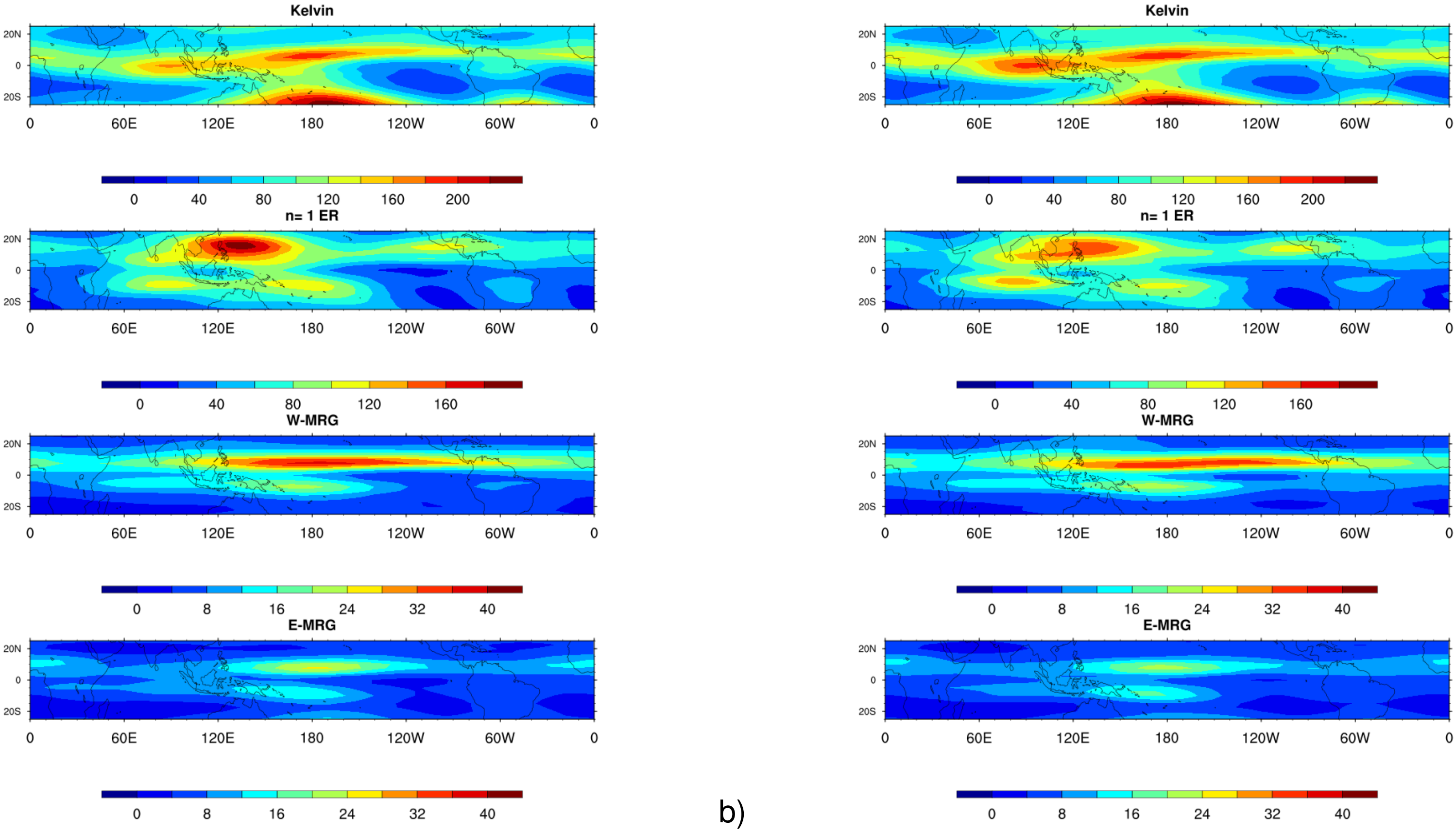

Figure 1.18: Mean variance of OLR during a)easterly and b)westerly phase of QBO for a period 1979-2011 is shown. E-MRG is EIG(n=0). All other waves retain the same name.

Chapter 2

Vertical Propagation of Convectively Coupled Equatorial Waves

2.1 Introduction: Vertical Propagation

Equatorial waves have been identified in the equatorial stratosphere in numerous observational analysis(Yanai and Maruyama 1966, Wallace and Kousky 1968) and they have also been studied in relation to convective forcing from the lower atmosphere (Wheeler and Kiladis 1999, Kiladis et al 2009, Yang et al 2003, Yang et al 2007). Equatorial waves are also thought to play an important role in the interaction between troposphere and stratosphere through vertical zonal momentum exchange.

QBO, which is one of the major modes of variability in the equatorial stratosphere, is driven by equatorial wave modes. These equatorial wave modes are also expected to be modulated by the different phases of QBO (Lindzen and Holton 1968, Baldwin et al 2001). Numerous studies have revealed that eastward momentum is provided by eastward propagating wave modes mainly Kelvin waves, while westward momentum is provided by westward propagating waves modes mainly Equatorial Rossby waves(n=1)(hereafter ER) and Mixed Rossby-Gravity waves(hereafter MRG)(Lindzen and Holton 1968, Baldwin et al 2001). Since earlier studies have revealed that these three wave modes are the major carriers of vertical momenta, we restrict our analysis to understand the roles played by these wave modes in vertical momentum transfer.

Most of the earlier reported studies on Kelvin and MRG in the lower stratosphere and upper troposphere were restricted by the limited availability of data sources (Baldwin et al, 2001) and the coarser resolution of wind data available like ERA-15. In this chapter, we have investigated the vertical propagation and circulation associated with these wave modes under different ENSO and QBO forcing using more recent reanalysis data products.

2.2 Theory: Vertical Propagation

Here we assume that the equatorial atmosphere is barotropic. This assumption allows us to separate out horizontal and vertical components from the set of governing equations. We end up with a set of equations governing momentum and mass conservation :

$$\frac{\partial u}{\partial t} - fv + \frac{\partial \phi}{\partial x} = 0 \tag{2.1}$$

$$\frac{\partial v}{\partial t} + fu + \frac{\partial \phi}{\partial y} = 0 \tag{2.2}$$

$$\frac{\partial u}{\partial x} + \frac{\partial v}{\partial y} + \frac{1}{\rho_0}\frac{\partial (\rho_0 w)}{\partial z} = 0 \tag{2.3}$$

$$\frac{\partial^2 \phi}{\partial t \partial z} + wN^2 = 0 \tag{2.4}$$

where w is the perturbation in vertical velocity, N^2 is the buoyancy frequency and all other symbols mean the same as explained in Chapter 1.

Now, like in Chapter 1, we assume that the wave solutions are zonally propagating but, we also give them a vertical wave number m to describe their vertical propagation.

This gives us:

$$\begin{bmatrix} u \\ v \\ w \\ \phi \end{bmatrix} = e^{\mathrm{z/2H}} \times \begin{bmatrix} \hat{u}(y) \\ \hat{v}(y) \\ \hat{w}(y) \\ \hat{\phi}(y) \end{bmatrix} \times exp[i(kx + mz - \nu t)], \qquad (2.5)$$

where ν is the frequency, capped quantities describe the meridional structures of *u*, *v*, *w* and ϕ, and *H* is mean scale height which is close to 7 km in the stratosphere.

This set of equations can now be solved in the same way explained in Chapter 1, if we assume that $m^2 >> \frac{1}{4H^2}$ and the resultant equation describing the meridional structure is identical to equation 1.6 if we set $gh_e = \frac{N^2}{m^2}$.

2.3 Equatorial Winds in the Stratosphere

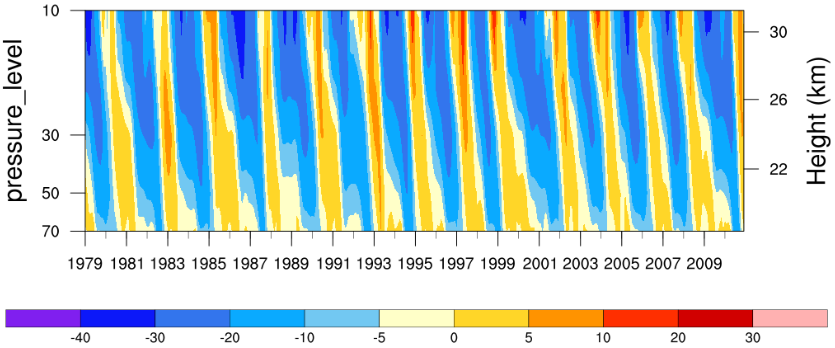

Figure 2.1: Time-height plot of mean equatorial zonal wind(monthly)(ms^{-1}) from 1979 to 2011 averaged in 15°S-15°N latitudes . Negative winds are easterlies and positive winds are westerlies. Pressure levels are in hPa.

Figure 2.1 shows the time-height plot of monthly averaged equatorial zonal winds from 1979 to 2011 between 10hPa and 70hPa. QBO is the major mode of variability of zonal winds in the equatorial stratosphere. This could be seen as downward moving easterly (negative) and westerly (positive) phases of zonal wind from the upper stratosphere to the lower stratosphere. QBO has a period of approximately 30 months and its phases are believed to be driven by the semi-annual oscillation which is dominant in the upper-stratosphere (Lindzen and Holton 1968).

Earlier studies indicated that Kelvin waves contribute largely towards the variability of equatorial zonal winds while *n=1* mode of ER waves and MRG waves contribute towards the variability of equatorial meridional winds in the middle atmosphere(Yang et al 2011, Yang et al 2012). In this study we follow a similar methodology and look for these wave contributions in the corresponding dynamic quantities. In order to do that, multi-level zonal and meridional wind data-sets were filtered for Kelvin, ER and westward propagating mode of MRG (WMRG) using their wavenumber, frequency and equivalent depth ranges obtained from spectral analysis (not shown).

Figure 2.2 shows the time-height plot of zonally averaged standard deviations of Kelvin, *n=1* ER and WMRG wave activities from 1979 to 2011 in the equatorial stratosphere (from 10hPa to 70hPa). Comparing with figure 2.1, we can see that Kelvin wave activity is stronger during the easterly phases of QBO, while *n=1* ER and WMRG wave activities peak during westerly phases of QBO. This shows how different phases of QBO, which is essentially determined by the direction of propagation of zonal winds in the equatorial stratosphere affect the vertical propagation of equatorial winds.

2.3.1 Zonal variation of equatorial wave activity

Figure 2.3 shows the height-longitude plot of meridionally (20°N- 20°S) averaged zonal winds, composited over all easterly (Fig. 2.3 left) and westerly (Fig. 2.3 right) phases of QBO. The easterly duct(concentration of strong easterly winds) in the eastern hemisphere (EH) and westerly ducts(concentration of strong westerly winds) in the western hemisphere (WH) near the tropopause is evident in both figures. In the stratosphere, as expected strong easterly winds are present during the easterly phase while westerly winds are present during the westerly phase. But there is not much longitudinal variation in either phases. Since not much is different in the lower-mid troposphere between the easterly and westerly phases of QBO, from here on we look for variations only in the upper troposphere and stratosphere during different phases of QBO. Figure 2.4 shows the height-longitude plots of wave activity of Kelvin, ER and WMRG

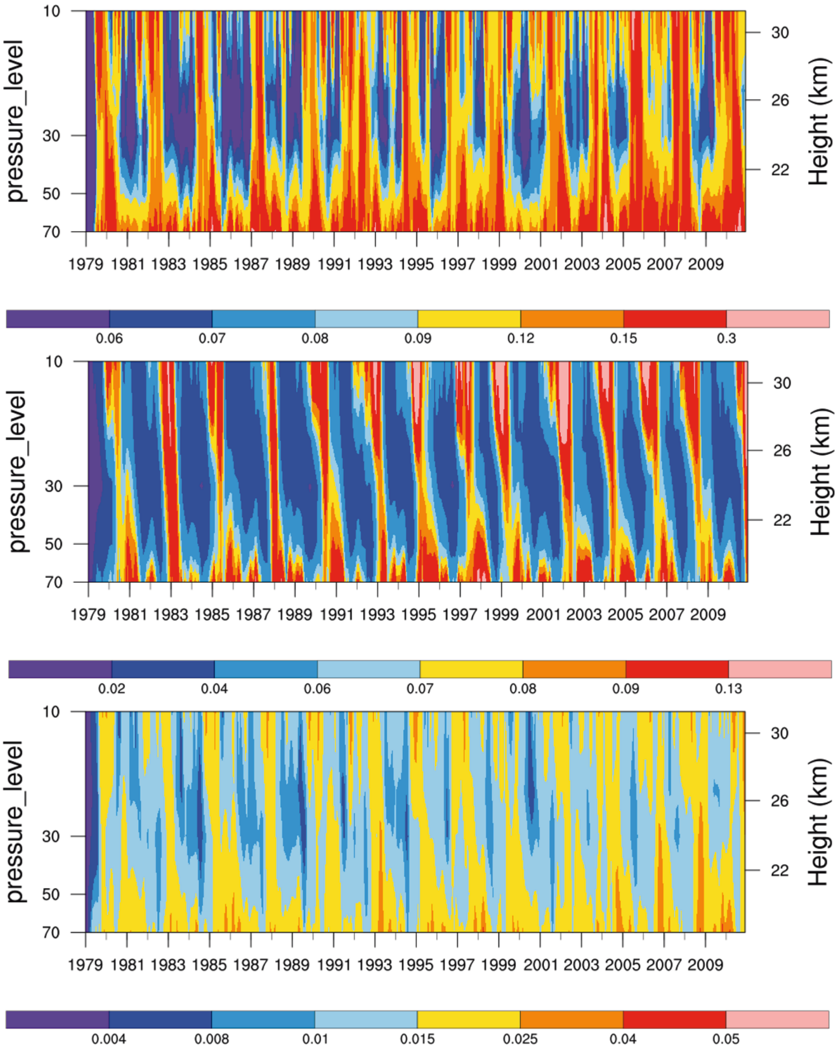

Figure 2.2: Time-height plot of zonally averaged standard deviations of (top) Kelvin wave in equatorial *u*, (middle) *n=1* ER in equatorial *v* and (bottom) WMRG in equatorial *v* from 1979 to 2011.

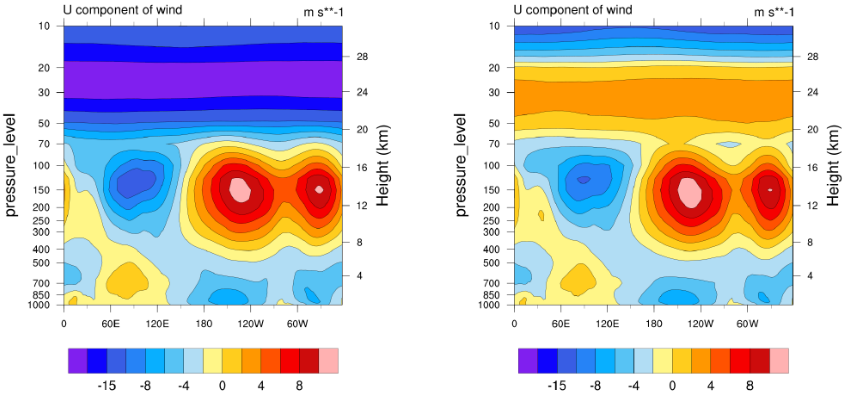

Figure 2.3: Height-longitude plots of equatorial zonal winds(ms^{-1}) averaged over all latitudes from 20°N to 20°S and over all years of (left) easterly phase of QBO and (right) westerly phase of QBO.

during easterly and westerly phases of QBO. In the stratosphere, all three waves have varied activities during the phases of QBO. Kelvin wave activity is clearly stronger during the easterly phase than in the westerly phase. It should also be noted that the stronger Kelvin wave activity during the easterly phase is mostly in the EH. In contrast, *n=1* ER and WMRG wave activities peak during the westerly phase of QBO. WMRG wave is stronger in the WH during the westerly phase of QBO. Earlier studies (Yang et al, 2012) indicated that *n=1* ER is stronger in the WH during westerly phase of QBO in 10-300 hPa region. However our analysis reveals that, although stronger during westerly phase of QBO, the increased activity of ER wave is only evident in the upper troposphere. Even during westerly phase of QBO, ER wave activity is quite uniform throughout the stratosphere.

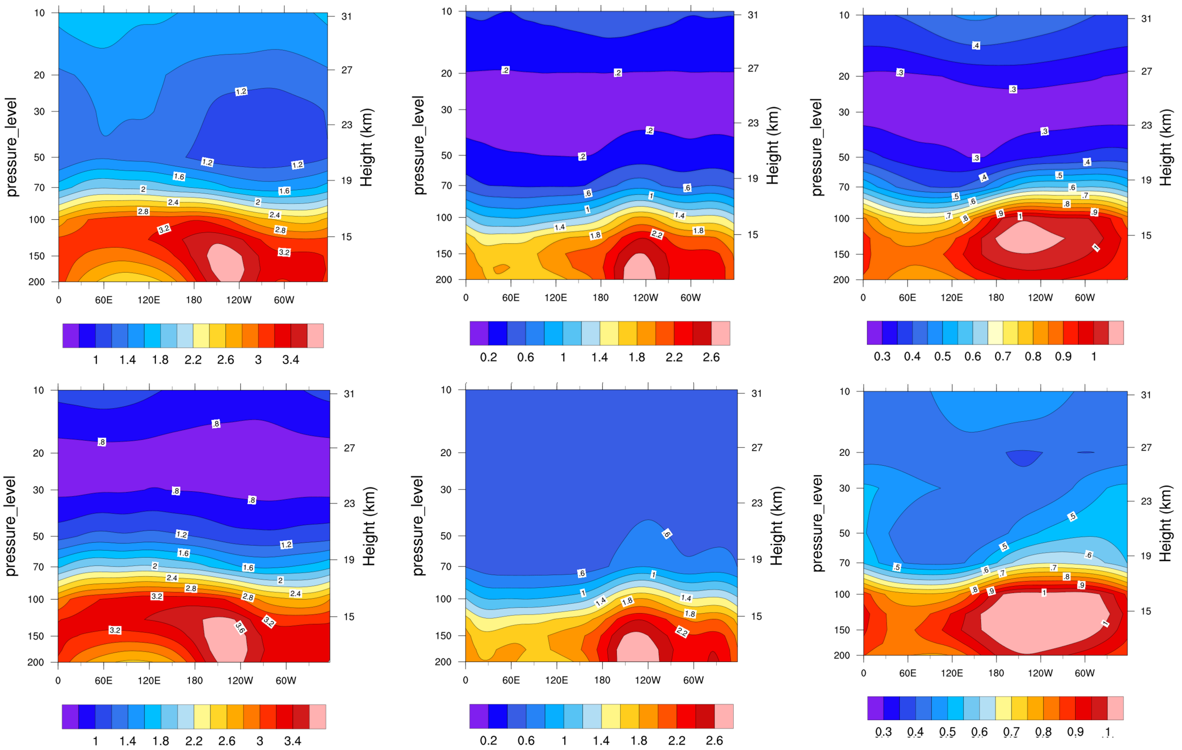

Figure 2.4: Height-longitude plots of standard deviations of Kelvin wave in *u*(left), *n=1* ER in *v*(middle) and WMRG in *v* averaged over (top panel) easterly phase and (bottom panel) westerly phase of QBO.

2.4 Equatorial winds in the Upper Troposphere

In this section, we study the impact of El-Nino and La-Nina phases on equatorial waves in the upper troposphere which would extend the analysis in Chapter 1 to the upper troposphere.

2.4.1 Zonal variation of equatorial wave activity

Figure 2.5 shows the height-longitude plots of meridionally (20°N to 20°S) averaged equatorial zonal wind composited over El-Nino and La-Nina phases. The most striking features are the stronger easterlies over the Indian ocean region and stronger westerlies over the mid-Pacific ocean region, during La-Nina in the upper troposphere. No major features or major differences between El-Nino and La-Nina phases are seen in the upper stratosphere which could mean that ENSO does not have a strong impact over the stratospheric processes. Figure 2.6 shows the height-longitude plots of wave activities of Kelvin, ER and WMRG during El-Nino and La-Nina phases. In the stratosphere, there is no significant differences between the wave activities during El-Nino and La-Nina phases. While in the upper troposphere, Kelvin and *n=1* ER wave activities peak during El-Nino phase while WMRG wave activity peaks during La-Nina. However, the highest variation in the wave activities of all three equatorial wave modes

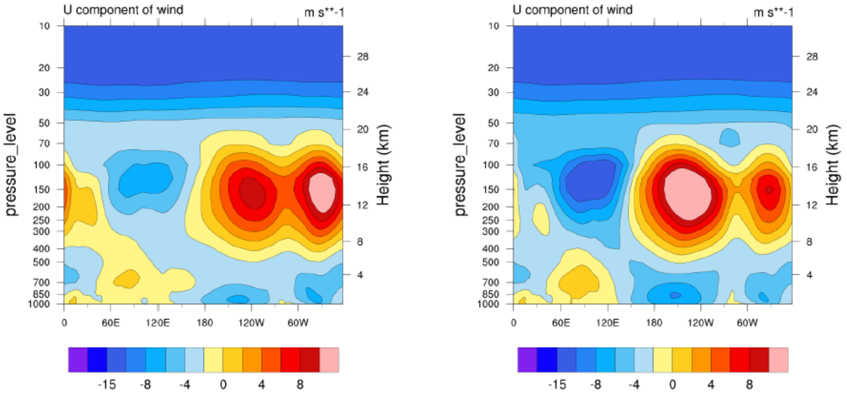

Figure 2.5: Height-longitude plots of equatorial zonal winds(ms^{-1}) averaged over all latitudes from 20°N to 20°S over all (left)El-Nino phase and (right)La-Nina phase of ENSO.

seem to more concentrated over the mid-Pacific region, in the upper troposphere. But it should also be noted that there is higher wave activity during preferred ENSO phases over the Indian ocean region. And a westward shift in the peak activity of westward propagating waves namely *n=1* ER and WMRG is also observed during La-Nina, which agrees with similar observations in Chapter 1.

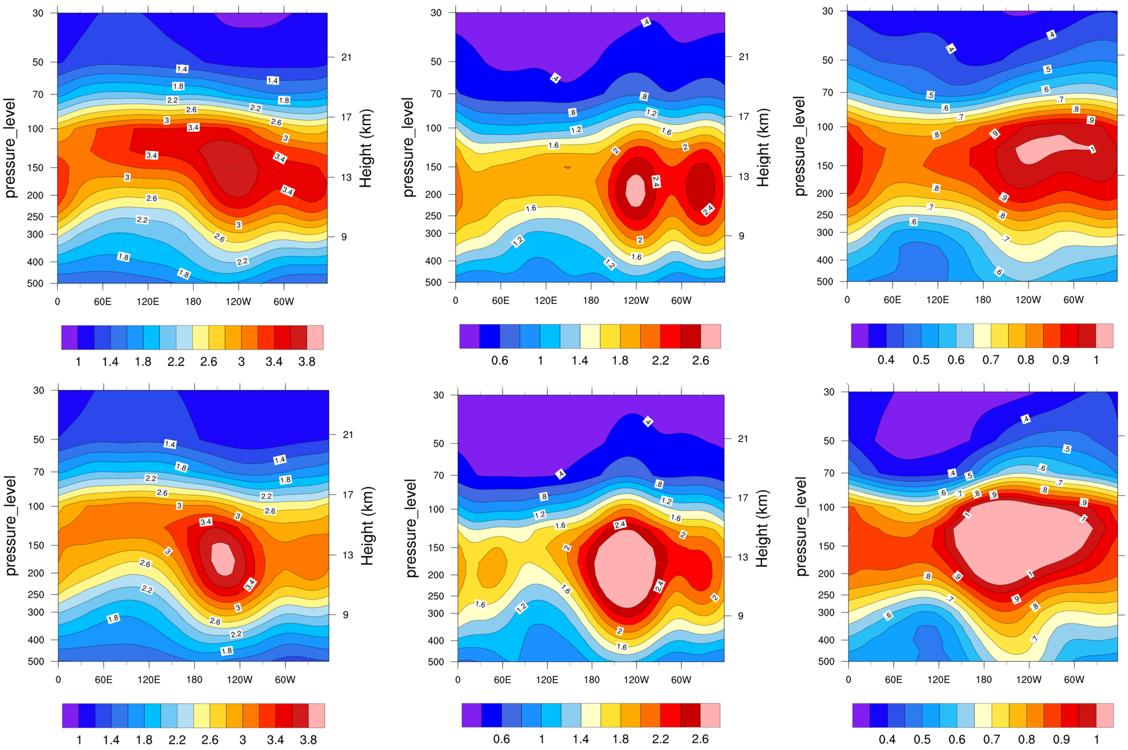

Figure 2.6: Height-longitude plots of standard deviations of Kelvin wave in *u*(left), *n=1* ER in *v*(middle) and WMRG in *v* averaged over (top panel)El-Nino and (bottom panel)La-Nina phases.

2.5 Equatorial Winds and Convection

Empirical orthogonal function (EOF) analysis of OLR data filtered for Kelvin, ER and WMRG waves was performed to obtain a reference time series. Zonal (for Kelvin) and meridional (for ER and WMRG) winds at multiple levels were regressed with this reference time series. This was done in a region between 15°N-15°S for all longitudes. Figure 2.7 shows the height-longitude plots of this analysis. Kelvin wave is filtered at zonal wavenumbers 2 - 10, ER is filtered for zonal wavenumbers 1-10 while WMRG is filtered for zonal wavenumbers 1-8. From the vertical structure of the regressed waves, it can be seen that Kelvin, ER and WMRG have varied locations of convection. The tilted vertical structures of these wave modes are consistent with earlier studies (Kiladis et al 2009, Roundy and Janiga 2012). Kelvin wave shows maximum convective activity in the Atlantic and Indian ocean region, ER largely in the western and central Pacific and WMRG mostly in the central Pacific. From figure 2.7 it can be inferred that these waves are convectively forced and from the results of Chapter 1 we have confirmed that these waves have shallower equivalent depths in the lower troposphere. Since earlier studies indicate that WMRG and Kelvin waves are found in the lower stratosphere and they propagate as dry waves which have higher equivalent depth (Kiladis et al 2009), we infer that the shallower equivalent depth of these wave modes in the lower troposphere is due to their coupling with convection.

2.6 Propagation of Kelvin, *n=1* ER and WMRG waves

Combined Empirical Orthogonal Function analysis was performed on wave-filtered OLR and zonal wind(for Kelvin) and meridional wind(for ER and WMRG) data at 850 hPa to obtain a reference time series. Wavenumber-frequency filtered OLR and unfiltered zonal and meridional winds at 850 hPa were regressed with the reference time series to obtain the OLR and wind patterns representative of Kelvin, ER and WMRG waves. The directions of propagation of Kelvin, ER and WMRG waves can be clearly seen in figure 2.8. The vectors represent the wind structure and the contours depict the OLR anomalies associated with the wave modes. The phase speed of these wave modes can also be understood from these plots.

2.6.1 Kelvin Wave

The most striking feature of Kelvin wave seen in the lead/lag plot is that the winds are mainly zonal very near to the equator. Also note that the 850 hPa winds are symmetric

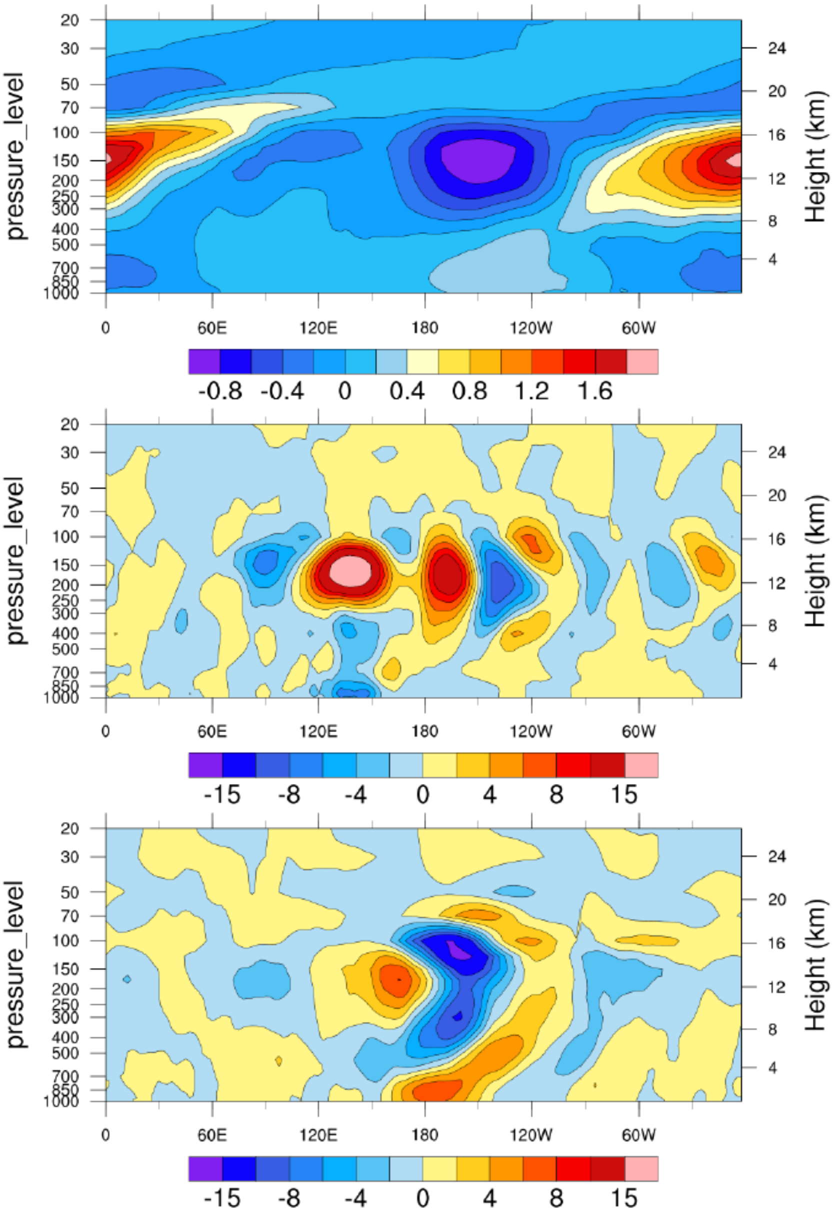

Figure 2.7: Height-longitude plots of (top)normalized U850 anomalies linearly regressed with normalized time series of EOF of OLR filtered for Kelvin wave, (middle) normalized V850 anomalies linearly regressed with normalized time series of EOF of OLR filtered for *n=1* ER wave and (bottom) normalized V850 anomalies linearly regressed with normalized time series of EOF of OLR filtered for WMRG wave. Pressure levels are in hPa.

very close to the equator. Both of these features are predicted by the SW theory. Although the wind structure is symmetric about the equator, the OLR anomaly is hardly symmetric about the equator. The negative contours show negative OLR anomaly, which indicates convection. It can also be seen that the winds at 850 hPa are westerly to the west and easterly to the east of the regions of convection indicating convergence. In Lag:-4 through Lag:+4 plots this entire pattern can be seen as propagating eastward at 10-15 ms^{-1}.

2.6.2 *n=1* ER wave

n=1 ER wave mode is symmetric about the equator and this is seen in figure 2.8(middle). The twin vortices that are anti-clockwise and clockwise in the Northern and Southern hemispheres respectively are one of the prominent features of this wave mode and it can be seen clearly in Lag:4 where it is over the central Pacific. The reason why it is not seen as clearly in the Eastern Pacific is because ER variance increases from Eastern Pacific to Western Pacific which was also seen in Figure 1.15 in Chapter 1. It is also interesting to observe that the vortices are not entirely over the convective region but rather slightly shifted to the west. It can also be seen from Lag:-8 through Lag:8 how, the southern part of ER variance weakens significantly as it reaches the Indian ocean region, which was also seen in Figure 1.15 in Chapter 1.

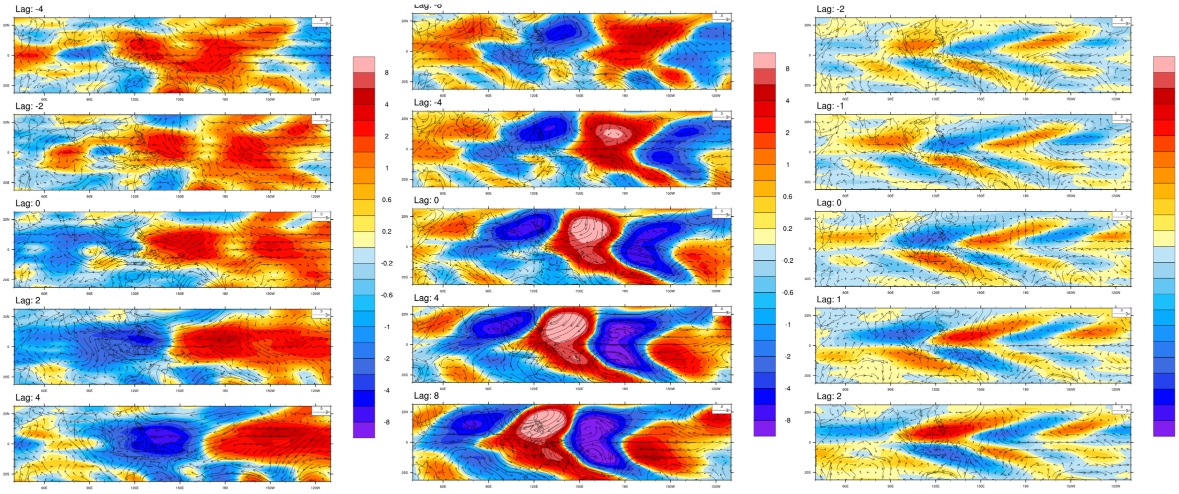

Figure 2.8: Propagation of (left) Kelvin, (middle) ER and (right) WMRG waves over a period of 8, 16 and 4 days respectively. The contours show the wave filtered OLR anomalies and the vectors indicate the velocity profile at 850 hPa.

2.6.3 WMRG wave

The antisymmetric OLR signal with gyres symmetric about the equator seen in Figure 2.8 (right) plots for WMRG matches fairly well with the theoretical predictions. As seen from Figure 1.15 in Chapter 1, WMRG variance is highest over the western-central Pacific region. It can also be seen that enhanced convection is associated with pole-ward winds while equator-ward winds are associated with suppressed convection.

2.7 Conclusions

We could make the following conclusions from the analysis in this chapter: 1) In the lower stratosphere and upper troposphere, Kelvin wave activity in zonal wind peaks during the easterly phase of QBO, while ER and WMRG wave activities in meridional wind peak during westerly phase of QBO. 2) The stronger Kelvin wave activity in the easterly phase of QBO happens in the EH, while the stronger WMRG wave activity in the westerly phase of QBO happens in the WH. However ER wave activity in the stratosphere peaks uniformly without zonal variation during westerly phase of QBO. 3) The easterlies in the EH and the westerlies in the WH in the upper troposphere are stronger during La-Nina phase of ENSO. 4) ENSO does not affect the wave activities of Kelvin, ER and WMRG in the stratosphere. However, El-Nino favors symmetric wave modes (Kelvin and ER) and La-Nina favors antisymmetric wave modes (WMRG) in the upper troposphere, which is consistent with the results of Chapter 1. 5) La-Nina favors a westward shift in the wave activities of westward propagating wave modes(ER and WMRG). However no such effect on Kelvin waves have been observed. These observations are also consistent with the results from Chapter 1. 6) The Kelvin and WMRG wave modes could be convectively forced which explains their shallower equivalent depths in the lower troposphere. 7) Kelvin, ER and Kelvin wave modes closely resemble the predictions by the Shallow Water Theory.

Chapter 3

Multi-Model Analysis

In this chapter we analyze OLR, U850 and U200 data from 5 global climate models namely, MPI-ECHAM6, MRI-AGCM, NCAR-CAM5, NCEPCPC-CFSv2 and SPCCSM, which are a part of the GEWEX Atmosphere System Study (GASS) and WCRP-WWRP/ THORPEX Year of Tropical Convection (YOTC) Activity and WGNE MJO Task Force, Global Model Evaluation Project, which shows good fidelity in simulating MJO, which are compared with observation results to see how well these models mimic the presence of CCEWs in the troposphere. All these models have been tested and are proven to model MJO efficiently (Jiang et al, 2015).

3.1 Wavenumber- frequency Spectral Analysis

Wavenumber- frequency spectral analysis was performed on all model data and wave activity for Kelvin (between eq. depth of 12m-100m) wave, ER and WMRG (between eq. depth of 12m-50m) waves are compared with the results obtained from observations. NINO3.4 index for each model was computed using model generated SST anomalies to identify El-Nino and La-Nina conditions. Since QBO phases are not correctly simulated by these models, a corresponding QBO index could not be calculated. Hence the following sections discuss the comparison of results obtained from various model data with observations under the influence of different phases of ENSO.

3.1.1 OLR

Figure 3.1 shows the comparison of average normalized power of Kelvin, ER and WMRG wave activities in OLR, between the model data-sets and the real data, under different mean states of ENSO. It can be seen that ER wave activity is well modelled in all models under all background conditions except MRI-AGCM which over estimates it. WMRG and Kelvin wave activities are well modelled in SPCCSM under all background conditions, while all other models significantly underestimate their signals. From the analysis in Chapter 1 and Chapter 2, we found higher activities of Kelvin and ER waves during El-Nino, while La-Nina preferred WMRG wave. These model data however, do not give the same results.

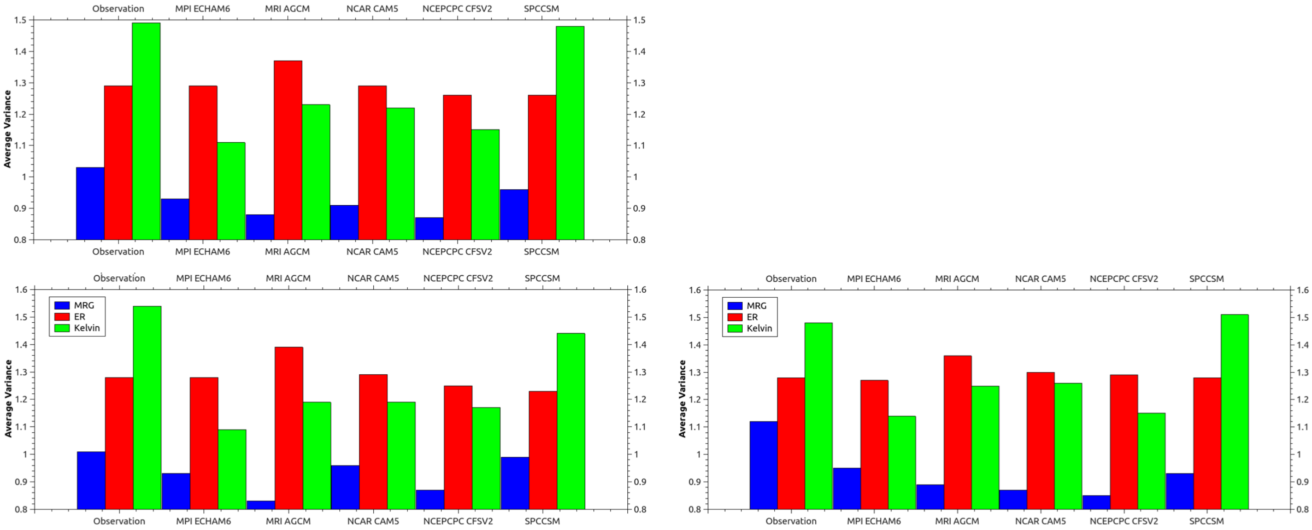

Figure 3.1: Average variance (normalized) of Kelvin, ER and WMRG waves in wavenumber-frequency plot of OLR, from 5 model data compared to observed data under different mean states: (top left) composite of all years from 1979-2011, (bottom left) composite of all El-Nino years and (bottom right) composite of all La-Nina years.

3.1.2 U850

Figure 3.2 shows the same analysis as in Fig. 3.1, but for U850. ER wave activity modelled by the models are comparable to observations. Both NCAR-CAM5 and SPCCSM model Kelvin wave activity better than other models. However, since WMRG wave signal is observed to be very weak in U850, nothing substantial could be said about the efficiency of any model in this regard. It is also worthwhile to note that Kelvin wave signals are modelled virtually identically between El-Nino and La-Nina phases while they observed to be slightly weaker during La-Nina.

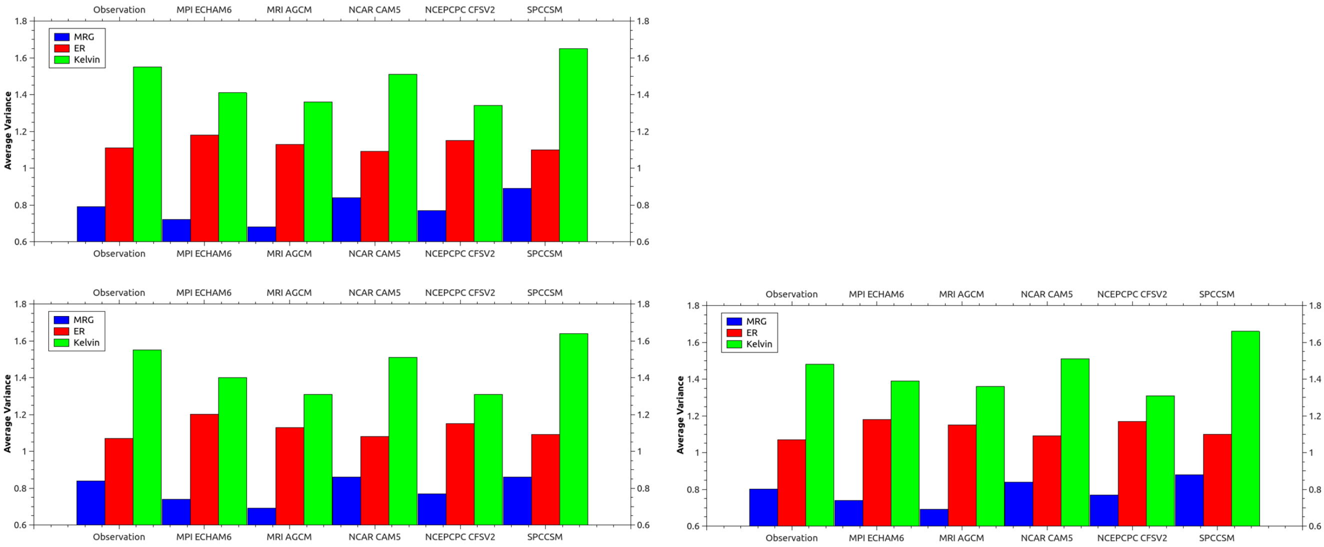

Figure 3.2: Same as Fig. 3.1, but for U850 data.

3.1.3 U200

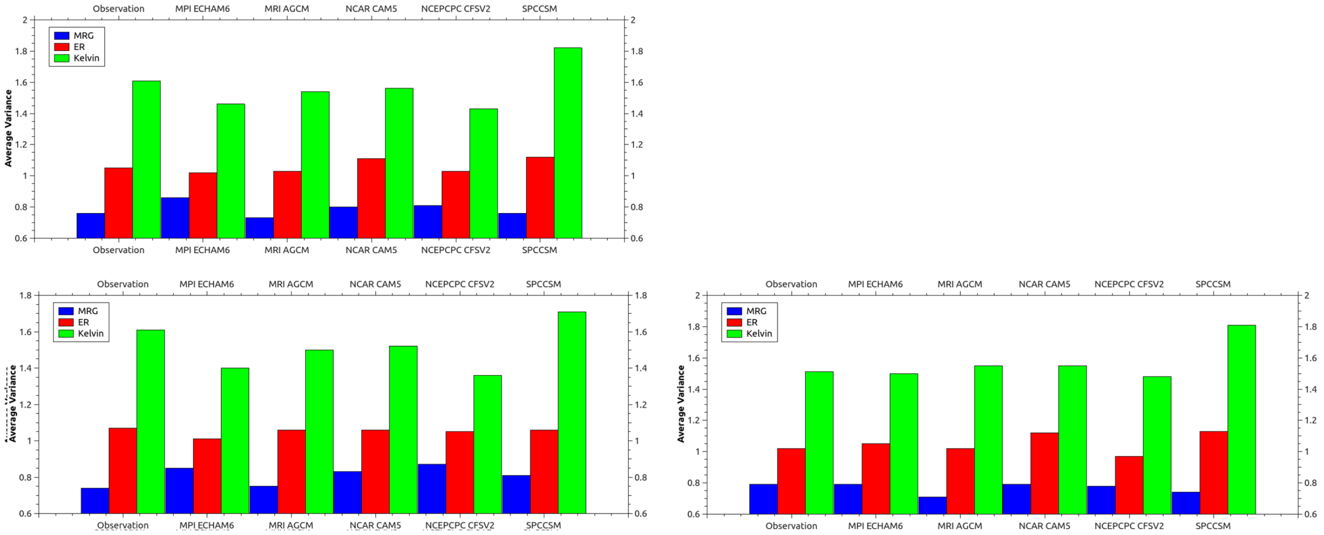

Figure 3.3: Same as Fig. 3.1, but for U200 data.

Figure 3.3 shows the same analysis as in 3.1, but for U200. Unlike in OLR model data, ER wave signals are modelled well by all models under all background conditions considered. While Kelvin wave signals are also modelled well, due to the presence of weak WMRG signals in U200 observations, nothing significant could be said about the efficiency of any model in simulating WMRG wave signals.

3.2 Coherence-squared spectral analysis

Since SPCCSM data best simulated Kelvin, ER and WMRG wave activities out of all the 5 models analyzed, we have analyzed the coherence squared spectra of OLR with U850 under different background conditions in SPCCSM. Table 3.1 summarizes the details of it.

Wave Type	'79-'11	El-Nino	La-Nina
Kelvin	0.425	0.525	0.425
ER	0.225	0.225	0.225
MRG	0.125	0.125	0.125

Table 3.1: The maximum coherence-squared values of OLR with u850 for different waves are shown for various mean states. All other details are the same as in Table 1.3.

From Table 3.1, we see increased coherence- squared values of OLR with U850 in Kelvin wave activity during El-Nino. However,correlation of OLR with U850 in WMRG wave and ER wave activities remain unchanged under different background conditions.

3.3 Spatial distribution of OLR variance

OLR data was wavenumber-frequency filtered for Kelvin, ER and WMRG in a similar procedure as explained in Chapter 1 and its spatial distribution of mean variance was analyzed. Figure 3.4 shows the spatial distribution of wave-filtered OLR variance for the five models. Comparing with figure 1.15 in Chapter 1, we observe that MRI AGCM, NCEPCPC CFSv2 and SPCCSM have modelled ER wave activity comparable to that in real data . MPI ECHAM6 and NCAR CAM5 overestimate ER wave activity.

Kelvin wave signals in all models except MRI AGCM and NCEPCPC-CFSv2 are comparable to what is observed in real data, while WMRG activities in all models except MRI AGCM and NCEPCPC CFSv2 are modelled well. The same analysis was done for periods of El-Nino and La-Nina based on NINO 3.4 index computed from model SST data, but no significant differences were observed between the two phases (not shown).

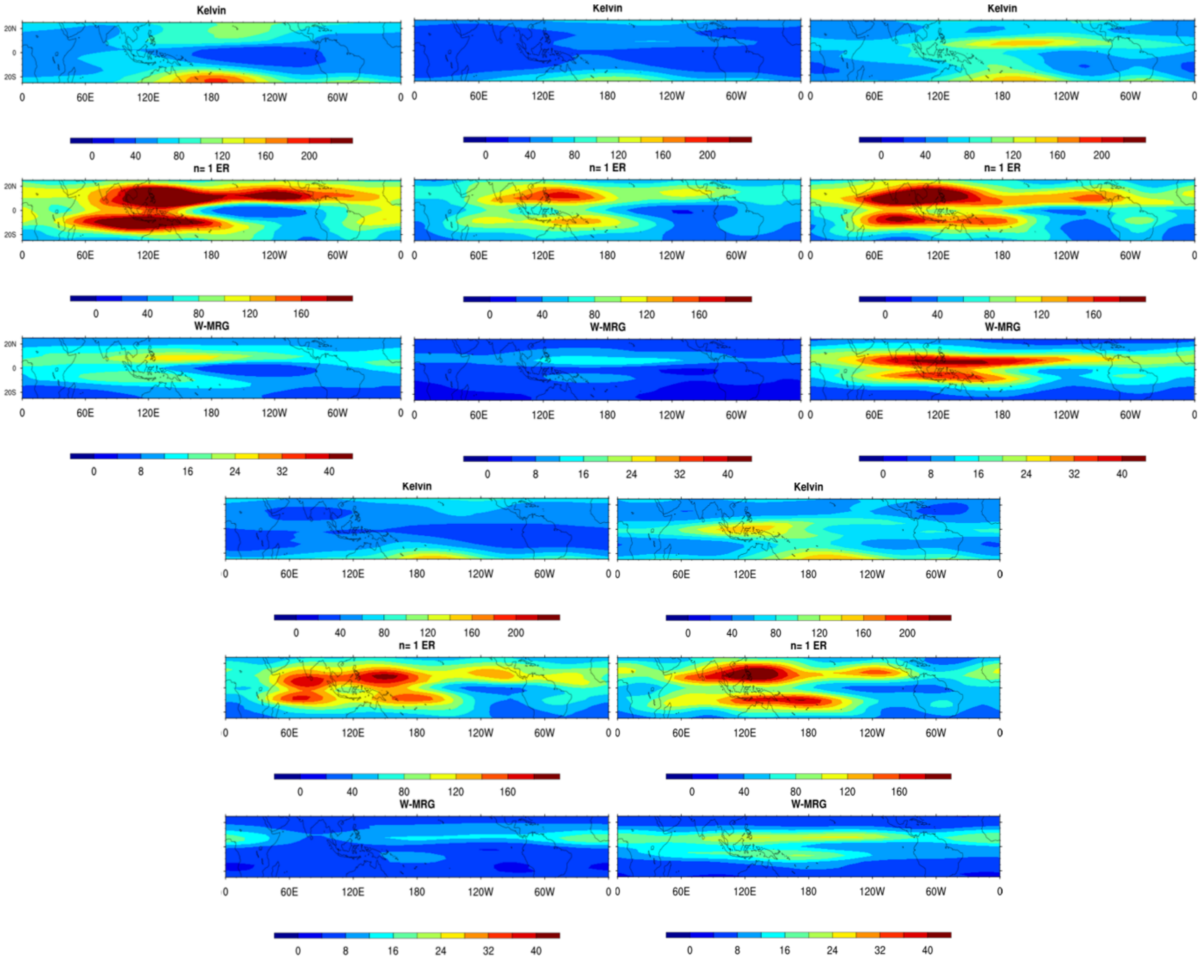

Figure 3.4: Spatial distribution of wave-filtered OLR variance of Kelvin wave, ER wave and WMRG wave in (top left) MPI-ECHAM6,(top middle) MRI-AGCM,(top right) NCAR-CAM5, (bottom left) NCEPCPC-CFSv2 and (bottom right)SPCCSM. The variances are plotted in a region of 25°N-25°S and all longitudes.

In case of WMRG wave activity, MPI-ECHAM6 and SPCCSM produce results that are closest to observations. However neither of these models simulate increased WMRG activity during any particular mean state.

3.4 Conclusions

We make the following conclusions from this multi-model analysis: 1) SPCCSM simulates Kelvin, ER and WMRG well in OLR. 2) There is no preferential peaking of activity of any wave during any background state. 3) OLR are U850 show high correlation between each other in SPCCSM for Kelvin, ER and WMRG, although WMRG had a weak signal in U850.

Major Conclusions

1)Symmetric wave modes are favored during El-Nino and anti-symmetric wave modes are more active during La-Nina.

2)The active zones of westward propagating wave modes in troposphere shift westward during La-Nina.

3)Kelvin wave activity peaks during easterly phase of QBO while ER and WMRG wave activities peak during westerly phase of QBO.

4)Among the five models, SPCCSM was found to be the most efficient in generating equatorial wave modes. However, none of the models were able to show any significant changes between different phases of ENSO.

Future Scope

1)It is found that ENSO affects the strength and locations of equatorial wave activities in the troposphere. But since the results in this study only provide an average picture, the effect of strength of ENSO events is not understood. So a detailed study emphasizing the effect of different ENSO events could possibly provide more consistent results.

2)This study has confirmed that different phases of QBO has a significant effect in the strengthening of different wave modes, indicating the importance of computing the vertical transfer of zonal momenta by different wave modes between troposphere and stratosphere. This could be further investigated in future studies.

3)The results in the third chapter show the ability of SPCCSM to efficiently simulate equatorial waves. Its also shown that the models were unable to simulate significant changes between different mean states. Since one of the models is able to generate equatorial waves very efficiently, it would interesting to work on methods to improve the models capability.

References

1) Matthew C. Wheeler, George N. Kiladis, 1999:*Convectively Coupled Equatorial Waves: Analysis of Clouds and Temperature in the WavenumberFrequency Domain, Journal of The Atmospheric Sciences, 56, 374-399.*

2)Harry H. Hendon, Matthew C. Wheeler,2008:*Some SpaceTime Spectral Analyses of Tropical Convection and Planetary-Scale Waves, Journal of The Atmospheric Sciences, 65, 2936-2948.*

3)Malcolm J. King, Matthew C. Wheeler, Todd P. Lane, 2015:*Association of Convection with the 5-Day RossbyHaurwitz Wave, Journal of The Atmospheric Sciences, 72, 3309-3321.*

4)George N. Kiladis, Matthew C. Wheeler, Patrick T. Haertel, Katherine H. Straub, Paul E. Roundy, 2009:*Convectively Coupled Equatorial Waves, Reviews of Geophysics, 47.*

5)Taroh Matsuno, 1966:*Quasi-Geostrophic Motions in the Equatorial Area, Journal of the Meteorological Society of Japan, 44, 25-43.*

6)Gui-Ying Yang, Brian Hoskins, Julia Slingo, 2003: *Convectively Coupled Equatorial Waves: A New Methodology for Identifying Wave Structures in Observational Data, Journal of Atmospheric Sciences, 60, 1637-1654.*

7)Gui-Ying Yang, Brian Hoskins, Julia Slingo, 2011: *Equatorial Waves in Opposite QBO Phases, Journal of Atmospheric Sciences, 68, 839-862.*

8)Gui-Ying Yang, Brian Hoskins, Lesley Gray, 2012: *The Influence of the QBO on the Propagation of Equatorial Waves into the Stratosphere, Journal of Atmospheric Sciences, 69, 2959-2982.*

9)Paul E. Roundy and Matthew A. Janiga, 2012: *Analysis of vertically propagating convectively coupled equatorial waves using observations and a non-hydrostatic Boussinesq model on the equatorial beta-plane, Quarterly Journal of the Royal Meteorological Society, 138, 1004-1017.*

10)J. C. Tindall, J. Thuburn and E. J. Highwood, 2005: *Equatorial waves in the lower stratosphere I: A novel detection method, Quarterly Journal of the Royal Meteorological Society, 132, 177-194.*

11)Yanai M. and T. Maruyama, 1966: *Stratospheric wave disturbances propagating over the equatorial Pacific. J. Meteor. Soc. Japan, 44, 291294.*

12)Wallace, J. M., and V. E. Kousky, 1968: *Observational evidence of Kelvin waves in the tropical stratosphere. J. Atmos. Sci., 25, 900907.*

13)Lindzen, R. S., and J. R. Holton, 1968: *A theory of the quasi-biennial oscillation. J. Atmos. Sci., 25, 10951107.*

14)Baldwin, M. P., and Co-authors, 2001: *The quasi-biennial oscilla- tion. Rev. Geophys., 39, 179229.*

15)Jiang, X., et al., 2015: *Vertical structure and physical processes of the Madden-Julian oscillation: Exploring key model physics in climate simulations, J. Geophys. Res. Atmos., 120, 4718 4748.*